Journal of Physics B:
Atomic, Molecular and
Optical Physics

Zinc Kβ *ab initio* diagram and satellite transitions

To cite this article: P H Dong *et al* 2026 *J. Phys. B: At. Mol. Opt. Phys.* **59** 045002

IOP Publishing J. Phys. B: At. Mol. Opt. Phys. 59 (2026) 045002 https://doi.org/10.1088/1361-6455/ae43d7

Journal of Physics B: Atomic, Molecular and Optical Physics

RECEIVED
27 October 2025

REVISED
20 January 2026

ACCEPTED FOR PUBLICATION
9 February 2026

PUBLISHED
24 February 2026

PAPER

Zinc Kβ *ab initio* diagram and satellite transitions

P H Dong, T V B Nguyen, S M Krstevski and C T Chantler[*]

School of Physics, The University of Melbourne, Parkville 3010, Australia
[*] Author to whom any correspondence should be addressed.

E-mail: chantler@unimelb.edu.au

Keywords: zinc Kβ, MCDHF, shake-off satellites, convergence metrics, Σ metric

Supplementary material for this article is available online

Abstract

Anomalies in the characteristic x-ray spectra of 3*d* transition metals, particularly in lineshape, linewidth, and intensity ratios, have long motivated detailed investigation. We present the first accurate *ab initio* study of the zinc Kβ spectrum, using multiconfiguration Dirac–Hartree–Fock. We predict the zinc Kβ spectrum, including the K$\beta_{1,3}$ diagram doublet together with the dominant satellite transition manifolds for the first time, from $[4s]$, $[3d]$, $[3p]$, and $[3s]$ single shake-off, as well as $[3d^2]$ double shake-off. Such features cannot be resolved by experiment as proven by the literature over several decades. We investigate two novel active space approaches. New convergence metrics are questioned and assessed for energy eigenvalues, gauge ratios A^L/A^V, transition A coefficients, and a newly developed Σ metric. We achieve energy eigenvalue convergence within 0.03 eV, gauge ratios A^L/A^V within 0.6%, convergence of transition A coefficients within 0.03% to 0.23%, and convergence of the Σ-metric to within 0.1% to 6.1%. *Ab initio* shake probabilities are used to quantify satellite contributions to experiment for the first time for zinc. Sequential inclusion of satellite components was evaluated in comparison with the most accurate data available, showing that all dominant shake transitions are required for an accurate description. Incorporating these satellites yields excellent agreement with experiment.

1. Advanced relativistic quantum theory

Transition studies in complex atomic systems serve as stringent tests for the formulation of advanced atomic models. Reconstructing experimental spectra from first principles is critical for validating our understanding of many-body quantum systems, relativistic quantum mechanics, and quantum electrodynamics (QED). Medium Z elements, particularly 3*d* transition metals, are of special theoretical interest; relativistic and QED effects are significant compared with lighter elements, whilst nuclear structure effects remain relatively small compared with heavier elements, providing a cleaner testbed for perturbative QED. Additionally, the partially filled *d*-shell introduces strong correlation, making these systems critical benchmarks for many-body theory.

Zinc holds a unique position as the terminal element within the 3*d* series, with closed 3*d* and 4*s* subshells in its ground state. Compared with its open shell neighbours, zinc offers a simpler electronic structure in which the valence 3*d* and 4*s* shell correlation is greatly suppressed and without additional complexity arising from open shell coupling. However, no modern relativistic calculation for zinc has been presented in the literature, and the only highly resolved experimental study remains that of Ito *et al* [1], leaving gaps in our understanding of the full spectral profile. A focused theoretical study of zinc thus provides a valuable reference point within the transition metals.

X-ray fluorescence spectra, especially the K lines and their satellite structures, provide detailed insights into atomic structure, electron correlation, and decay dynamics. These spectra are central to fundamental atomic physics, encompassing radiative and non-radiative (Auger) decays, transition rates, and level lifetimes, while also supporting a wide range of applications in astrophysics [2, 3], plasma physics [4], material science [5], geoscience [6], and biology [7].

Charles Barkla first observed both the K spectra and L spectra [8]. Henry Moseley defined the periodic table by the relationship between the characteristic Kα spectral energies and frequencies, with atomic number Z, based upon the number of protons [9], and was also able to plot separated Kα, Kβ, and Lα, Lβ, and Lγ energies.

Various mechanisms have been proposed to explain the origin of these satellites, including shake processes [10–12], Auger and Coster–Kronig transitions [13], plasmon excitations [14, 15], and Kondo-like interactions [16]. In this work, we focus on the role of shake processes in shaping the observed spectral features.

Despite extensive theoretical efforts, experimental observations of K-line spectra in $3d$ transition metals continue to reveal discrepancies from standard predictions of relativistic quantum mechanics including the Breit interactions and QED contributions. Key discrepancies and anomalies include the asymmetrical line-shape [17], the $I(K\alpha_2)/I(K\alpha_1)$ intensity ratio [18] and the spectral linewidths [18, 19]. These deviations indicate the presence of additional physical processes beyond conventional theory. Even more challenging are the possible existence of satellite transition energies lying energetically close to the main diagram lines, often masked by broadening or experimental resolution, which are beginning to provide compelling explanation for asymmetries [20–23]. The overlap of these unresolved features contributes to the characteristic asymmetric profiles of Kα and Kβ emission spectra.

Among the $3d$ transition metals, the Kβ_1 and Kβ_3 peaks, unlike their Kα_1 and Kα_2 counterparts, cannot be resolved experimentally into distinct peaks due to the small energy separation between transitions and the natural lifetimes and widths. The dominant K$\beta_{1,3}$ lines arise from bound-bound $[1s] \rightarrow [3p]$ transitions, where the square brackets denote hole states, with the energy emitted as a Kβ photon. The energies are split due to angular momentum coupling between the hole orbital. Within the jj-coupling scheme, the initial state involves a coupling of a hole with the $1s$ orbital, forming a singlet $\{1s_{1/2}\}$, while the final state consists of a coupling of a hole with the $3p$ orbital, producing a doublet $\{3p_{1/2}, 3p_{3/2}\}$. This leads to two transitions, $[1s_{1/2}] \rightarrow [3p_{3/2}]$ $(K\beta_1)$ and $[1s_{1/2}] \rightarrow [3p_{1/2}]$ $(K\beta_3)$, with an energy separation of only a few eV. This splitting, however, is small compared with the intrinsic lifetime broadening, causing the individual spectral lines to overlap and merge into a single, unresolved feature. Consequently, purely experimental approaches are insufficient for resolving the fine structure of the zinc Kβ emission line, underscoring the need for accurate theoretical calculations.

For zinc Kβ, the target for this work, the presence of an additional hole in an outer nl shell perturbs the electrostatic environment of the core and the $3p$ orbitals, so that the resulting $[1snl] \rightarrow [3pnl]$ transition is shifted by a few eV related to the diagram $[1s] \rightarrow [3p]$ Kβ decay, producing spectral features that are experimentally unresolved. Although unresolvable as discrete peaks, these satellites play a crucial role in shaping the apparent asymmetry and broadening of the observed K$\beta_{1,3}$ spectrum, and thus must be considered for a complete description of transition metal spectra.

Calculations involving only the diagram K$\beta_{1,3}$ transitions fail to account for the observed asymmetries in the experimental spectrum. We present a comprehensive analysis that includes, in addition to the diagram lines, contributions from satellite transitions associated with single shake processes involving the $[4s]$, $[3d]$, $[3p]$, and $[3s]$ subshells, as well as double shake transitions involving $[3d^2]$. These additional contributions are essential for accurately reproducing the spectral shape and understanding the many-body dynamics in the emission process.

2. Multiconfiguration Dirac–Hartree–Fock (MCDHF) method

Determination of the zinc Kβ spectrum requires a precise calculation of the initial and final state atomic wavefunctions. Here, we follow MCDHF method, where a relativistic product wave-function is given by the product state of N Dirac orbitals. Each one-electron orbital takes the form:

$$\langle \mathbf{r}|n,\kappa,m\rangle = \phi_{n\kappa m}(\vec{r}) = \frac{1}{r}\begin{pmatrix} P_{n\kappa}(r)\,\Omega_{\kappa m}(\theta,\phi) \\ i\,Q_{n\kappa}(r)\,\Omega_{-\kappa m}(\theta,\phi) \end{pmatrix}$$

where ϕ is the 4 component Dirac spinor, $P(r)$ and $Q(r)$ are the large and small radial components, respectively, and $\Omega(\theta,\phi)$ is the two component spinor angular function. The radial components satisfy the normalisation condition,

$$\int_0^\infty \left[|P_{n\kappa}(r)|^2 + |Q_{n\kappa}(r)|^2\right]\mathrm{d}r = 1. \tag{1}$$

Each of the product electron configuration state functions (CSFs) needs to be constructed for fermions, using the antisymmetrisation operator $\mathcal{A}$:

$$\Phi(\mathbf{r}_1,\mathbf{r}_2,\ldots,\mathbf{r}_N) = \mathcal{A}\left[\prod_{i=1}^{N}\phi_i(\mathbf{r}_i)\right]. \tag{2}$$

The atomic-state function (ASF), Ψ, is represented as the linear combination of CSFs, where each CSF has well defined atomic parity, angular quantum numbers and magnetic quantum number,

$$\Psi_\alpha(\Pi JM) = \sum_r c_r(\alpha)\,\Phi(\gamma_r \Pi JM). \tag{3}$$

The degeneracies of the electronic configuration is specified by γ_r. The radial wavefunctions associated with each CSF and the mixing coefficients c_r follow the Dirac-Coulomb Hamiltonian [24–28].

In our MCDHF implementation, we employ GRASP [28–30]. Transverse photon interactions, QED corrections (self-energy, vacuum polarisation), and finite nuclear mass effects are included as perturbations. In particular, the self-energy is evaluated using the LCG-Welton method [28, 30].

3. *Ab initio* probability and the relation to the Kβ spectrum

For the purposes of reference spectra, and calibration emission characteristic spectra, we require that the incident energy is far above (e.g. three times) the (K) edge energy. Then the sudden or impact approximation is valid, as the ejection time of the 1*s* photoelectron is much shorter than the characteristic relaxation time of the remaining atomic electrons. Within the MCDHF framework, the probability of a shake-off event (total shake) occurring in a given $n\kappa$ subshell is expressed as [22, 31, 32]:

$$P^{\text{shake}}_{n\kappa} = 1 - \left| \sum_j c_j d_j \langle \phi_{n\kappa} | \tilde{\phi}_{n\kappa} \rangle^{M_{n\kappa}} \right|^2 \tag{4}$$

where the inner product involves the one electron orbitals $\phi_{n\kappa}$ and $\tilde{\phi}_{n\kappa}$ corresponding to the relaxed and unrelaxed atomic states, respectively, after photoionisation of the 1*s* electron. This overlap is weighted by the configuration mixing coefficients c_j and d_j. Here, $M_{n\kappa}$ is the electron occupation number of the subshell. The orbital overlap is evaluated from the radial components of the Dirac orbitals,

$$\int_0^\infty \left[P_{n\kappa}(r)\,\tilde{P}_{n\kappa}(r) + Q_{n\kappa}(r)\,\tilde{Q}_{n\kappa}(r)\right] \mathrm{d}r. \tag{5}$$

Equation (4) describes the probability that a shake-off occurs within a subshell, but it does not specify how many electrons are ejected from that subshell, nor does it account for shake events in other subshells. Assuming that each electron in a given subshell has an equal probability of being shaken off, the per-electron shake-off probability is

$$q = 1 - \left(1 - P^{\text{shake}}_{n\kappa}\right)^{\frac{1}{M_{n\kappa}}} \tag{6}$$

so that the number of shaken electrons X from the subshell follows a binomial distribution $X \sim \mathrm{Bi}(M_{n\kappa}, q)$:

$$P_{n\kappa}(X = k) = \binom{M_{n\kappa}}{k} \left[1 - \left(1 - P^{\text{shake}}_{n\kappa}\right)^{\frac{1}{M_{n\kappa}}}\right]^k \times \left(1 - P^{\text{shake}}_{n\kappa}\right)^{\frac{M_{n\kappa}-k}{M_{n\kappa}}}. \tag{7}$$

Equation (7) allows us to define single shake ($X = 1$), double shake ($X = 2$) and total shake ($X \geqslant 1$) probabilities for each subshell. To describe shake processes at the atomic level, the state of all subshells must be specified simultaneously, which we refer to as the isolated (joint) shake-off probability. In the sudden limit, where shake events in different subshells are uncorrelated, the isolated (joint) shake-off probability is simply the product of the subshell contributions. For example, the probability of an isolated 4*s* shake-off (a single 4*s* electron being shaken off from the atom with no shake in any other subshell) is [32, 33]

$$P\left(4s^1\right) = P_{1,-1}(X = 0) \times \cdots \times P_{3,-3}(X = 0) \times P_{4,-1}(X = 1). \tag{8}$$

Ab initio shake probabilities are summarised in table 1. The predominant shake-off processes involve the 4*s* subshell and the 3*d* subshell, resulting in $4s^1$ and $3d^9$ satellite transitions, each with a probability on the order of 14%. The $3p^5$ transition contributes around 7%, followed by $2p^5$, and $3s^1$. The probability of no shake-off occurring, corresponding to the diagram transition, is estimated by subtracting the summed shake-off probabilities of the dominant channels from unity, or is estimated from the binomial theorem by requiring $P_{n\kappa}(X = 0)$ for all subshells. This provides an estimation of the relative population of singly K-shell ionisation and multiple K-, M-shell ionisations contributing to the Kβ spectrum.

Table 1. Zn Kβ: Total, single and double shake probabilities (%) for a given $n\kappa$ subshell and for the corresponding nl subshell, following [33]. Probabilities are obtained from equation (7), with $P_{n\kappa}(X \geqslant 1)$ for the first two rows, $P_{n\kappa}(X = 1)$ for the next two rows, and $P_{n\kappa}(X = 2)$ for the last two rows. Calculations employ wavefunctions expanded to the 5g level. Note these shake probabilities double count processes and include multiple shakes from other sub-shells.

nl	1s	2s	2p		3s	3p		3d		4s
jj-Coupling terms	$1s_{1/2}$	$2s_{1/2}$	$2p_{1/2}$	$2p_{3/2}$	$3s_{1/2}$	$3p_{1/2}$	$3p_{3/2}$	$3d_{3/2}$	$3d_{5/2}$	$4s_{1/2}$
n, κ total shake	2.295	2.357	2.463	2.542	2.693	3.070	3.740	6.114	8.055	13.716
nl total shake	2.295	2.357	5.005		2.693	6.810		14.168		13.716
n, κ single shake	2.295	2.343	2.448	2.517	2.675	3.046	3.687	5.970	7.776	13.211
nl single shake	2.295	2.343	4.965		2.675	6.733		13.745		13.211
n, κ double shake	0.000	0.014	0.015	0.024	0.018	0.024	0.053	0.142	0.274	0.506
nl double shake	0.000	0.014	0.101		0.018	0.189		0.881		0.506

Table 2. Zn Kβ: Isolated single shake probability (%) from any particular $n\kappa$ subshell calculated using analogues of equation (8), together with the total shake probabilities for the $n\kappa$ subshell from table 1. These formulae do not double-count and represent amplitudes for each discrete satellite spectrum.

n, κ	$1, -1$	$2, -1$	$2, 1$	$2, -2$	$3, -1$	$3, 1$	$3, -2$	$3, 2$	$3, -3$	$4, -1$
jj-Coupling terms	$1s_{1/2}$	$2s_{1/2}$	$2p_{1/2}$	$2p_{3/2}$	$3s_{1/2}$	$3p_{1/2}$	$3p_{3/2}$	$3d_{3/2}$	$3d_{5/2}$	$4s_{1/2}$
n, κ Isolated single shake	1.441	1.472	1.539	1.584	1.686	1.927	2.349	3.899	5.186	9.390
nl	1s	2s	2p		3s	3p		3d		4s
nl Isolated single shake	1.441	1.472	3.123		1.686	4.276		9.085		9.390

Table 3. Estimated relative intensities of the dominant transitions, normalised to the Zn Kβ spectrum, following tables 2 and [33]. These values give relative intensities between different transition manifolds.

	Diagram	$4s^1$	$3d^9$	$3p^5$	$3s^1$	$3d^8$
Isolated probability (%)	61.327	9.390	9.085	4.276	1.686	0.605
Normalised ratio (%)	71.0	10.8	10.5	5.0	2.0	0.7

The resulting probabilities for the isolated single satellite spectra are given in table 2. Here only one shake process is permitted, for the particular $n\kappa$ subshell listed. These isolated single shake probabilities are, less than the total shake probabilities. Specifically, the probabilities of isolated single shakes are given in order for 4s (9.4%); 3d (9.1%); 3p (4.3%); 2p (3.1%); 3s (1.7%) and 2s (1.5%) in order of magnitude. The $n = 2$ shake-off spectra are significantly higher in energy than the main Kβ spectrum, so can be neglected in the following discussion.

The resulting probabilities for the isolated double satellite spectra are provided in [33]. These isolated double shake probabilities are smaller as befits a second-order process. We focus herein on the $3d^2$ double shake process as typifying double shake processes and representing a complex transition spectrum, quite distinct from the single shake spectra.

The resulting probabilities for the diagram and predominant isolated satellite spectra to be investigated herein are summarised in table 3. These probabilities are derived from fully relativistic calculations, in which the satellite transitions are computed in the $n\kappa$ basis. For clarity in interpreting the spectra, however, the contributions are grouped and labelled according to the corresponding nl quantum numbers of the shake subshell, as the transition multiplet spectra are most naturally associated with nl.

Perhaps surprisingly, this theory predicts the probability of the diagram transition spectrum as only $P(D) = 61.3\%$, much lower than all past experimental analyses and theoretical predictions. Read on as we develop a proof of this, at least to first order. At this point, we note promisingly that all of the shake-off probabilities, including that for no-shake—i.e. the diagram spectra—sum to unity.

4. Approach to convergence

Electron orbital are determined variationally using the self-consistent field (SCF) method, implemented in GRASP. Open-shell and core-ionised systems are particularly prone to ’false convergence’ - that is, where the iterative procedure reaches apparent numerical stability while converging to an unintended or unphysical state. In practice, different choices of basis sets, initial orbital estimates, or optimisation algorithms can lead to calculation inconsistencies and compromising the predicted energies and transition parameters. A careful and systematic optimisation strategy is therefore required, in which the wavefunction is constructed progressively, shell by shell.

Correlation effects are included through configuration expansion (equation (3)) [33]. An active space (AS) approach for virtual orbitals enhances the stability of wavefunctions and convergence whilst retaining dominant correlation contributions. The strategy applied in this work is as follows:

1. Single and double (*SD*) excitations: up to two electrons are allowed to be excited from the restricted AS into the restricted virtual orbitals. The virtual orbital set is systematically enlarged from $4s \rightarrow 4f$, $4f \rightarrow 5s$, $5s \rightarrow 5g$, etc such that convergence of transition energies and amplitudes can be monitored at each stage of expansion.
2. Atomic symmetry conservation expansion: Only configurations with the same atomic parity Π, total angular momentum J, and projection M_J as the reference configuration are included, which captures radial correlation from the AS.
3. The double expansion accounts for pairwise electron-electron correlation within the AS.

The single configuration (no excitations) serves as the starting point and provides an approximation to the ASF. Systematic inclusion of *SD* excitations with larger set of CSFs refines the wavefunction for the eigenvalues. At the end of expansion, the initial and final state wavefunctions are biorthogonalised and the transition matrix can be evaluated.

Obtaining well-converged wavefunctions for open-shell systems is challenging. At the configuration interaction (CI) stage, convergence issues often manifest as nonphysical expansion coefficients from: (i) energetic, near-degenerate states due to spin-orbital coupling, making the orbital occupied in the Fock matrix ambiguous; (ii) limitations of the finite basis set, which reduce the accuracy of Hamiltonian diagonalisation in the relativistic CI procedure; (iii) the variational optimisation, where the Lagrange multipliers in the SCF calculation may converge to a local rather than global minimum, especially with a poor initial iteration; (iv) numerical limitations of the finite-difference method, where the radial grid may fail to resolve sharp variation in radial wavefunctions.

In multiconfiguration expansions, keeping the $1s2s2p$ core inactive has been shown to give stable results for zinc Kα transitions [33]. For the zinc Kβ transition, we find that the $3p$ shell must also be kept inactive. Two approaches with different ASs are investigated herein: ASs of $\{3d4s\}$ and separately ASs of $\{3s3d\}$. The enlargement of the restricted virtual orbital space increases the size of the CSF set, hence giving a closer approximation to the atomic state function. As the array of virtual orbitals is extended, the additional correlation corrections should become progressively smaller. The quality of wavefunctions and convergence are then examined through several key metrics.

5. Convergence metrics

5.1. Peak and weighted eigenenergies metric

To assess convergence of the spectrum, we monitor the evolution of transition energies as the AS is progressively enlarged. As the configuration space grows, the number of CSFs increases rapidly, while the additional higher-order corrections to the energy typically become marginal. The convergence criteria are therefore defined in terms of the relative changes in selected observables becoming sufficiently small.

We introduce two complementary metrics for convergence of the transition energies [33–36]: (i) the *peak energy*, E_{peak}, defined as the eigenenergy of the transition with the highest weighted oscillator strength (g_f) [34], and (ii) the *centre-of-mass energy* [35], defined as the intensity-weighted average of all contributing eigenenergies,

$$E_{\text{CoM}} = \frac{1}{\mathcal{N}} \sum_{i}^{n} E_i \left(g_f\right)_i , \tag{9}$$

where $\mathcal{N} = \sum_i^n (g_f)_i$ is the normalisation constant.

The variation of E_{CoM} across successive expansions quantifies the shift of the spectral centroid, while the stability of E_{peak} indicates the convergence of the most probable transition energy. Sufficiently small changes in both measures serve as necessary conditions for convergence [23, 35]. Ideally, E_{CoM} will be more sensitive to lack of convergence than E_{peak}.

5.2. Length to velocity ratio (A^V/A^L) metric

The evaluation of the electric dipole ($E1$) transition operator can be performed in the velocity or length form, corresponding to the non-relativistic limit of the Coulomb and Babushkin gauges, respectively [37]. Exact non-relativistic wavefunctions yield identical results in the two forms. However, in many-body calculations, discrepancies often arise. Agreement between the matrix elements in the two forms serves as a necessary but insufficient criterion for assessing the quality and convergence of the wavefunctions [34, 38]. To quantify this, the transition probability ratio, A^L/A^V, is obtained from the length and velocity values. Ratios approaching unity indicate a consistency between the two gauges. This metric has been implemented in precise atomic calculation for decades [34, 35, 39, 40].

Each transition manifold involves more than one transition, so rather than cataloguing each transition, we also define and introduce an average transition probability ratio,

$$A^L_{\text{ave}}/A^V_{\text{ave}} = \frac{\sum_i A^L_i}{\sum_i A^V_i}. \tag{10}$$

The variation of the individual ratios A^L_i/A^V_i about the average value is less then 0.1% within a given manifold in this work. Therefore, the average ratio is reported as a sufficient metric.

5.3. Transition A^L coefficient metric

In addition to the energy-based metrics, convergence is also assessed through the radiative transition rates. Transition A coefficients directly determine the intensities of spectral lines. Their stability across successive expansions offers independent measures of convergence. Two representative quantities are considered: (i) the *peak A coefficient*, A_{peak}, corresponding to the most radiatively probable transition within a manifold, and (ii) the *centre-of-mass A coefficient*:

$$A_{\text{CoM}} = \frac{1}{\mathcal{N}} \sum_i^n A_i \left(g_f\right)_i, \tag{11}$$

with normalisation constant $\mathcal{N} = \sum_i^n (g_f)_i$. Tracking A_{peak} and A_{CoM} complements the energy-based metrics, define an orthogonal axis of convergence of satellite spectra, and are necessary criteria for convergence. Convergence of A coefficients are given in appendix.

5.4. Radiative lifetime invariance (Σ Metric)

Recent studies of electric-dipole-allowed transition amplitudes and A-coefficients in copper Kα [36], zinc Kα [33] and scandium have identified a sensitive and robust metric associated with each $E1$ transition: the total theoretical transition rate, defined as the sum of all $E1$ rates for the core transition $[1s] \to [2p]$:

$$\Sigma\left([1s], J, lvl\right) = \sum_{J', lvl'} A\left([1s], J, lvl; [2p], J', lvl'\right) \tag{12}$$

where J is the atomic angular momentum, lvl (level) distinguishes configurations yielding the same J, and A is the $E1$ transition rate. The square brackets denote hole states as usual. This total rate was found to remain effectively constant for a given element, independent of the initial atomic state (J, level), and robust even in the presence of additional M- or N-shell spectator holes that form satellite manifolds. In other words, $\Sigma([1s], J, lvl) \approx \Sigma([1snl], J', lvl')$. This metric appears robust and sensitive in 3d elements including Cu, Zn and Sc.

Building on this concept, we extend the same invariance principle to the Kβ transition, $[1s] \to [3p]$. For clarity, we denote $\Sigma([1snl], J, lvl) = \Sigma_{nl}(J, lvl)$. For each nl shake-off transition, we define the ratio of the total dipole transition rate of a satellite line to that of the corresponding diagram line as:

$$\Sigma_S/\Sigma_D = \frac{\sum_i A_i\left(\text{satellite}\right)}{\sum_j A_j\left(\text{diagram}\right)} \tag{13}$$

where A_i denotes the transition A coefficient for a $[1s] \to [3p]$ transition to a final state i. Here, Σ_S and Σ_D represent the total $E1$ transition rates of the satellite and diagram transitions, respectively. The Σ ratio thus provides a normalised measure of radiative lifetime invariance across different initial configurations. Deviation of Σ ratio from unity often indicates a false convergence or missing transition eigenenergies.

6. Theoretical eigenenergies and transition amplitudes

Neutral zinc has a closed-shell configuration. Following photonionisation of a 1s electron, the most prominent electric dipole transitions result in Kα and Kβ lines, with an intensity ratio of about 7:1. The

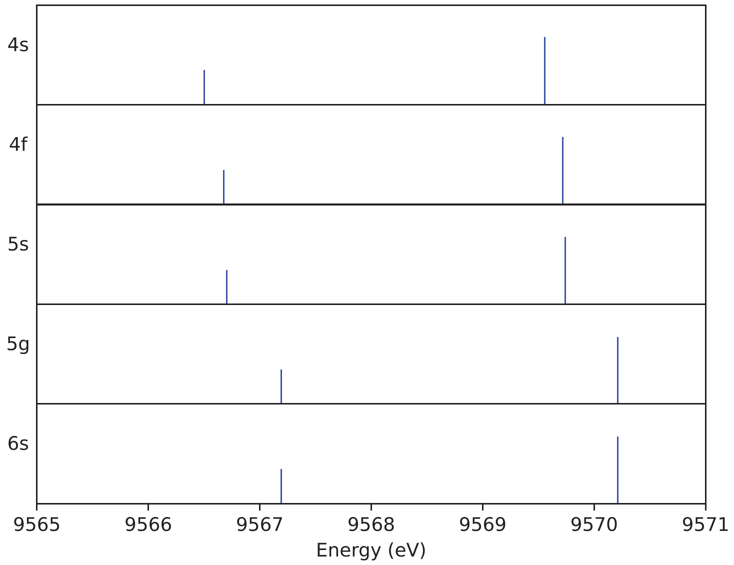

Figure 1. Zinc K$\beta_{1,3}$ diagram spectrum using active space 1 $\{3d4s\}$, with configuration expansions up to the 6*s* orbital. Each vertical line marks an eigenenergy, and its height indicates the relative transition intensity.

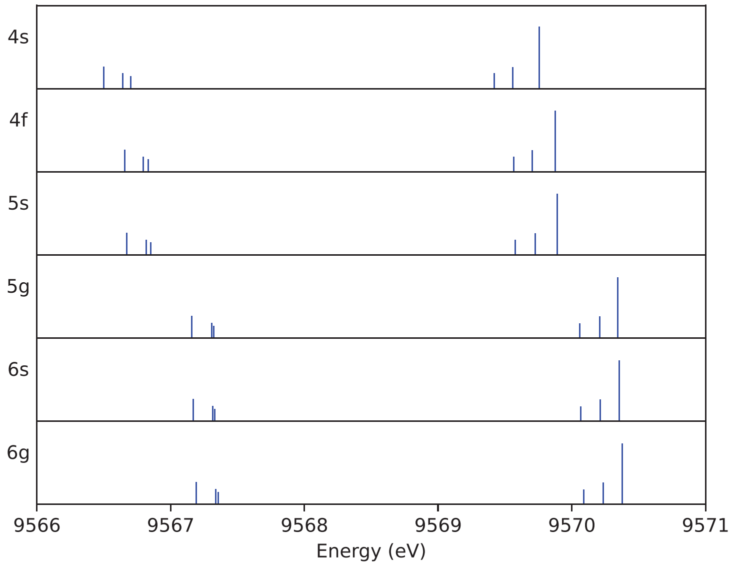

Figure 2. Zinc Kβ 4s^1 satellite eigenenergy spectrum using active space 1 $\{3d4s\}$. Additional pronounced energy shift appears at the 5*g* expansion, at the inclusion of important CSFs. Beyond this, the spectrum stabilises, and by the final 6*g* expansion, the residual shift is converged to below 0.03 eV.

canonical Kβ diagram transition corresponds to the electron configurations $\{1s^1 2s^2 2p^6 3s^2 3p^6 3d^{10} 4s^2\}$ for initial state and $\{1s^2 2s^2 2p^6 3s^2 3p^5 3d^{10} 4s^2\}$ for the final state. Near-degenerate shake-off satellites arise when additional vacancies present in the M- or N- shells of both the initial and final states. For example, the 3*d* single shake-off ($3d^9$) satellite involves configurations $\{1s^1 2s^2 2p^6 3s^2 3p^6 3d^9 4s^2\}$ and $\{1s^2 2s^2 2p^6 3s^2 3p^5 3d^9 4s^2\}$ for the initial and final states, respectively.

Both AS expansions, $\{3d4s\}$ and $\{3s3d\}$, were employed to calculate all of the diagram and dominant satellite spectra, including 4*s*, 3*d*, 3*p*, and 3*s* single shake-off as well as 3*d* double shake-off transitions. The $\{3d4s\}$ expansion includes the diagram transition and the 4*s*, 3*d* and 3*s* single shake-off satellites, while the $\{3s3d\}$ expansion covers the 3*d* and 3*p* single shake-off and the 3*d* double shake-off satellites (figures 1–7), in order of predicted significance.

6.1. Results using $\{3d4s\}$ AS expansion

The diagram transition consists of just two eigenenergies, $E(\mathrm{K}\beta_1)$, $E(\mathrm{K}\beta_3)$, since all other subshells are closed. Table 4 provides eigenenergies and A^L/A^V gauge ratios for each level of expansion, calculated

Table 4. Theoretical zinc Kβ diagram transitions, presenting expansions up to the 6s level using active space 1 $\{3d4s\}$. The gauge ratio A^L/A^V involves the A coefficient computed using the dipole operator in the length (Babushkin) and velocity (Coulomb) gauges. Excellent convergence of the diagram eigenvalues is seen to 0.01 eV, with the separation of $E(K\beta_1) - E(K\beta_3)$ converging to 3.02(1) eV. The gauge ratio converges to 1.006, or 0.6%.

Zinc K$\beta_{1,3}$ diagram transitions calculated with active space 1 $\{3d4s\}$			
Expansion		Kβ_1 $J = \frac{1}{2} \rightarrow \frac{3}{2}$	Kβ_3 $J = \frac{1}{2} \rightarrow \frac{1}{2}$
4s	Energy (eV)	9569.56	9566.50
	A^L/A^V	1.0059	1.0061
4f	Energy (eV)	9569.72 ($\pm$0.16)	9566.68 ($\pm$0.17)
	A^L/A^V	1.0059	1.0061
5s	Energy (eV)	9569.74 ($\pm$0.02)	9566.70 ($\pm$0.03)
	A^L/A^V	1.0059	1.0061
5g	Energy (eV)	9570.21 ($\pm$0.47)	9567.19 ($\pm$0.49)
	A^L/A^V	1.0060	1.0062
6s	Energy (eV)	9570.22 ($\pm$0.01)	9567.20 ($\pm$0.01)
	A^L/A^V	1.0060	1.0062

Table 5. The two diagram transitions in Zn K$\beta_{1,3}$ originate from the same initial atomic J and initial level. Hence the decay lifetime and partial width is 0.29 eV (using active space 1 $\{3d4s\}$), significantly smaller than the experimental scale of a few eV. This result is used later as a new metric for convergence.

Total dipole radiative rate for Zn Kβ diagram transitions (Σ_D) with active space 1 $\{3d4s\}$			
Initial J	Initial level	$\Sigma_D(10^{14}s^{-1})$	Partial radiative FWHM (eV)
$\frac{1}{2}$	1	4.425	0.291

using the $\{3d4s\}$ expansion. The fine structure splitting for the diagram transitions is $E(\mathrm{K}\beta_1) - E(\mathrm{K}\beta_3) = 3.02(1)$ eV, with gauge ratios close to unity. Corresponding transition energies, $E(\mathrm{K}\beta_1) = 9570.22$ eV and $E(\mathrm{K}\beta_3) = 9667.20$ eV are in agreement with the $\{3s3d\}$ expansion within 0.05 eV. Since the diagram transition involves one initial state and two final states, the total transition rate Σ_D is obtained by summing the rates for $\{1s_{1/2}\} \rightarrow \{3p_{1/2}, 3p_{3/2}\}$. This yields $\Sigma_D = 4.42 \times 10^{14}\,s^{-1}$ from the $\{3d4s\}$ expansion (table 5), in excellent agreement with the result using $\{3s3d\}$ expansion (table 11. The total Kβ diagram rate, Σ_D, serves as the reference against which all satellite transition rates are compared for the Σ metric.

For the 4s^1 satellite, the absence of a 4s electron introduces further angular momentum coupling between subshells. The initial configuration has two possible atomic angular momenta, $J_i \in \{0, 1\}$, while the final configuration allows four, $J_f \in \{0, 1^{(1)}, 1^{(2)}, 2\}$, where the superscript distinguishes the two distinct atomic configurations (levels) that both yield $J_f = 1$. Hence there are six independent eigenenergies for the allowed $E1$ transitions. Table 6 lists the corresponding eigenenergies and A^L/A^V ratios. The transition energies group into two clusters near 9570 eV (cluster 1) and 9567 eV (cluster 2). These clusters overlap strongly with the diagram lines Kβ_1 and Kβ_3, and their relative intensities closely mirror the diagram intensity ratio $I(\mathrm{K}\beta_1)/I(\mathrm{K}\beta_3)$. This strong spectral overlap makes it extremely difficult to experimentally resolve the 4s^1 lines from the main diagram transitions [41].

The 4s^1 satellite comprises two initial upper states, $J_i = 0$ and $J_i = 1$. For $J_i = 0$, the total transition rate, obtained by summing over $0 \rightarrow \{1^{(1)}, 1^{(2)}\}$, is $\Sigma_{4s^1}(J_i = 0) = 4.43 \times 10^{14}\,\mathrm{s}^{-1}$. For $J_i = 1$, summing over $1 \rightarrow \{0, 1^{(1)}, 1^{(2)}, 2\}$ yields $\Sigma_{4s^1}(J_i = 1) = 4.43 \times 10^{14}\,\mathrm{s}^{-1}$. Both totals agree with the diagram transition rate Σ_D within 0.1% (table 7).

The 3s^1 satellite, figure 3, shows a partial lack of convergence yielding four visible eigenvalues out of six by symmetry. The four observed transition eigenvalues appear converged. The peak and centre-of-mass metrics for the energy eigenvalues, gauge ratios and A coefficients metrics also converge.

Table 8 summarises centre-of-mass energies, E_{CoM}, and average gauge ratios, $A^L_{\mathrm{ave}}/A^V_{\mathrm{ave}}$, for all satellite transitions using the $\{3d4s\}$ expansion, with more comprehensive tabulation of convergence criteria in appendix. The centre-of-mass energies converge within 0.02 eV at the highest level of expansion, except for the 3d^8 satellites, which vary by approximately 0.2 eV. All average gauge ratios converge to unity within 0.7%. The transition rates A_{peak} and A_{CoM} also converge within 0.1%, except for the 3d^8 satellites, for which A_{peak} appears converged while A_{CoM} shifts by about 5% at the highest expansion level (appendix). The total $E1$ transition rates of all satellites, Σ_S, are compared with the diagram transition

Table 6. Relativistic quantum mechanical zinc Kβ $4s^1$ satellite transition spectrum using active space 1 $\{3d4s\}$. For the final expansion, all eigenenergy shifts remain below 0.03 eV, and the A^L/A^V gauge ratios are close to unity.

Convergence criteria for zinc Kβ $4s^1$ satellite transition calculated with active space $\{3d4s\}$							
		Cluster 1 (near β_1)			Cluster 2 (near β_3)		
Expansion		$J=0\rightarrow1$	$J=1\rightarrow1$	$J=1\rightarrow2$	$J=0\rightarrow1$	$J=1\rightarrow0$	$J=1\rightarrow1$
$4s$	Energy (eV)	9569.56	9569.42	9569.76	9566.64	9566.70	9566.50
	A^L/A^V	1.0058	1.0059	1.0059	1.0060	1.0061	1.0061
$4f$	Energy (eV)	9569.71 (±0.15)	9569.57 (±0.15)	9569.87 (±0.11)	9566.79 (±0.15)	9566.83 (±0.13)	9566.65 (±0.15)
	A^L/A^V	1.0059	1.0060	1.0059	1.0061	1.0062	1.0062
$5s$	Energy (eV)	9569.72 (±0.01)	9569.58 (±0.01)	9569.89 (±0.02)	9566.82 (±0.03)	9566.85 (±0.02)	9566.67 (±0.02)
	A^L/A^V	1.0059	1.0060	1.0059	1.0061	1.0062	1.0062
$5g$	Energy (eV)	9570.21 (±0.49)	9570.06 (±0.48)	9570.34 (±0.45)	9567.31 (±0.49)	9567.32 (±0.47)	9567.16 (±0.49)
	A^L/A^V	1.0060	1.0061	1.0060	1.0062	1.0063	1.0063
$6s$	Energy (eV)	9570.21 (±0.00)	9570.07 (±0.01)	9570.35 (±0.01)	9567.31 (±0.00)	9567.33 (±0.01)	9567.17 (±0.01)
	A^L/A^V	1.0060	1.0063	1.0060	1.0062	1.0063	1.0063
$6g$	Energy (eV)	9570.24 (±0.03)	9570.09 (±0.02)	9570.38 (±0.03)	9567.34 (±0.03)	9567.35 (±0.02)	9567.19 (±0.02)
	A^L/A^V	1.0060	1.0061	1.0060	1.0062	1.0063	1.0063

Table 7. Σ metric application to the $4s^1$ satellite spectrum, using active space 1 $\{3d4s\}$. The decay rates A converge to within 0.1% of that for the diagram transition.

Total dipole radiative rate for Zn Kβ $4s^1$ transitions (Σ_{4s^1}) with active space 1 $\{3d4s\}$				
Initial J	Initial level	Σ_{4s^1} ($10^{14}s^{-1}$)	Partial radiative FWHM (eV)	Σ_{4s^1}/Σ_D
0	1	4.426	0.291	1.000
1	1	4.429	0.292	1.001

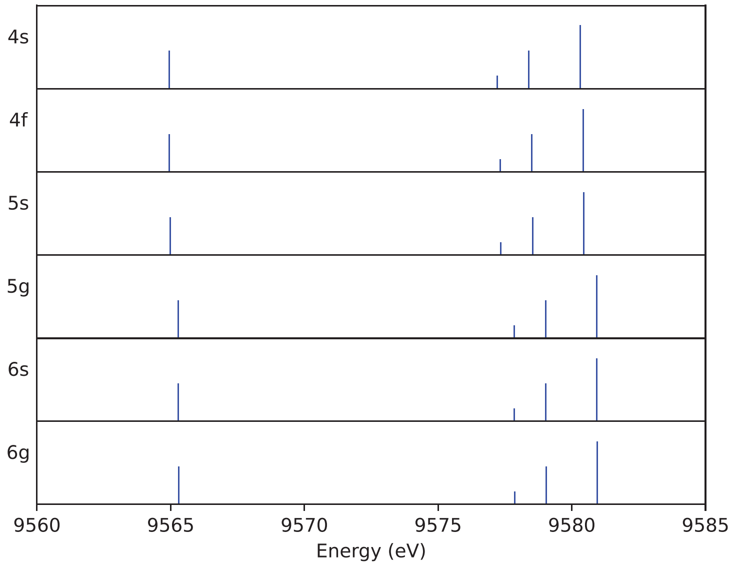

Figure 3. Zinc Kβ $3s^1$ satellite spectrum calculated using active space 1 $\{3d4s\}$ with expansion up to $6g$ orbital. The $3s^1$ transition yields six eigenenergies by symmetry, as with $4s^1$. However, two have oscillator strengths nearly two orders of magnitude smaller and are therefore not visible.

Table 8. Key convergence criteria for zinc Kβ satellite transitions using active space 1 $\{3d4s\}$ for energy and gauge. The transition probabilities are in excellent agreement in the two gauges. Eigenenergy shifts are below 0.02 eV, except for the $3d^8$ satellite, which shows incomplete convergence.

Convergence criteria for zinc Kβ satellite transitions calculated with active space 1 $\{3d4s\}$						
		Satellite				
Expansion		$4s^1$	$3d^9$	$3p^5$	$3s^1$	$3d^8$
$4s$	E_{CoM} (eV)	9568.62	9570.28	9574.92	9575.72	9572.95
	$A^L_{\mathrm{ave}}/A^V_{\mathrm{ave}}$	1.0060	1.0060	1.0049	1.0071	1.0060
$4f$	E_{CoM} (eV)	9568.76	9570.74	9574.97	9575.80	9573.93
		($\pm$0.14)	($\pm$0.46)	($\pm$0.05)	($\pm$0.08)	($\pm$0.98)
	$A^L_{\mathrm{ave}}/A^V_{\mathrm{ave}}$	1.0060	1.0060	1.0049	1.0071	1.0062
$5s$	E_{CoM} (eV)	9568.78	9570.76	9574.98	9575.83	9573.96
		($\pm$0.02)	($\pm$0.02)	($\pm$0.01)	($\pm$0.03)	($\pm$0.03)
	$A^L_{\mathrm{ave}}/A^V_{\mathrm{ave}}$	1.0060	1.0060	1.0049	1.0071	1.0062
$5g$	E_{CoM} (eV)	9569.25	9571.16	9575.22	9576.26	9573.77
($5d$ for $3d^8$)		($\pm$0.47)	($\pm$0.40)	($\pm$0.24)	($\pm$0.44)	($\pm$0.19)
	$A^L_{\mathrm{ave}}/A^V_{\mathrm{ave}}$	1.0061	1.0061	1.0050	1.0072	1.0061
$6s$	E_{CoM} (eV)	9569.26	9571.17	9575.22	9576.2	—
		($\pm$0.01)	($\pm$0.01)	($\pm$0.00)	($\pm$0.01)	—
	$A^L_{\mathrm{ave}}/A^V_{\mathrm{ave}}$	1.0061	1.0061	1.0050	1.0072	—
$6g$	E_{CoM} (eV)	9569.28	—	9575.22	9576.29	—
		($\pm$0.02)	—	($\pm$0.00)	($\pm$0.02)	—
	$A^L_{\mathrm{ave}}/A^V_{\mathrm{ave}}$	1.0061	—	1.0050	1.0072	—

rate Σ_D in table 9. The $4s^1$ satellite rates agree with the diagram remarkably well, and the $3s^1$ satellites agree within 3%. The $3d$, $3p$ and $3d^2$ satellite transitions do not reach $\Sigma_S/\Sigma_D \approx 1$, so we investigate alternate AS expansions.

6.2. Comparisons with AS 2: $\{3s3d\}$ expansion

Figures 4 ($\{3d4s\}$) and 5 ($\{3s3d\}$) show spectra of the prominent $3d^9$ satellite lines, using both AS expansions. In the previous $\{3d4s\}$ expansion, some eigenenergies near 9560 eV and 9567 eV vanish during the expansion. These eigenenergies are preserved at all levels in the $\{3s3d\}$ expansion. The $3p^5$ spectra are similar in both expansions (figure 6 ($\{3s3d\}$). For the $3d^8$ satellites, most eigenenergies are preserved in the $\{3s3d\}$ expansion (figure 7).

The centre-of-mass energy convergence and average gauge ratio convergence for the transitions in AS 2 $\{3s3d\}$ are given in table 10 and appendix. Convergence is excellent for both energy and gauge ratios, except for the $3s^1$ satellite, which exhibits a significant energy shift of 35.02 eV at the $4f$ level of expansion. Table 11 shows both the $3d^9$ and $3d^8$ satellites have Σ_S/Σ_D ratios approaching unity, with $3d^9$ converging within 3% and $3d^8$ within 6%. The $3p^5$ satellite exhibits a similar Σ_S/Σ_D ratio across both expansions. By contrast, the $3s^1$ satellite shows poor behaviour, with $\Sigma_{3s^1}(J=0)/\Sigma_D$ collapsing to zero, indicating a false convergence.

The diagram, $4s^1$, and $3p^5$ satellite spectra show strong consistency across both AS expansion schemes (figure 1 for the diagram, figure 2 for $4s^1$, and figure 6 for $3p^5$). Their peak energies and transition rates converge closely between the two approaches. For all three configurations, both E_{peak} and E_{CoM} agree within 0.09 eV, while A_{peak} and A_{CoM} differ by no more than 0.22% at worst (tables 18 and 19 in appendix).

In contrast, the $3d^9$, $3s^1$, and $3d^8$ satellites exhibit more pronounced discrepancies between the expansion schemes. Within the $3d4s$ expansion, several eigenenergies associated with the $3d^9$ and $3d^8$ transitions are suppressed during multiconfiguration coupling (figure 4) For $3d^9$, the peak energy agrees within 0.08 eV and A_{peak} within 0.016%, but the centre-of-mass energy deviates by 0.3 eV and A_{CoM} by about 20%. Similar behaviour is observed for $3d^8$, where energy differences remain below 0.5 eV while A_{CoM} deviates by more than 20% (tables 18 and 19 in appendix).

The $3s^1$ transition shows the most substantial divergence. In the $\{3s3d\}$ expansion, the $3s^1$ satellites undergo energy shifts on the order of tens of eV following multiconfiguration expansion, resulting

Table 9. Active space 1 $\{3d4s\}$ total $E1$ radiative rates for Zn Kβ satellite transitions (Σ_S), and the application of Σ metric. Rates for $4s^1$ and $3s^1$ satellite transitions agree with diagram decays within 3%; $3p$, $3d$ and $3d^2$ rates do not pass this metric.

Total dipole radiative rate for Zn Kβ satellite transitions (Σ_S) with active space 1 $\{3d4s\}$					
Configuration	Initial J	Initial level	$\Sigma_S(10^{14}s^{-1})$	Partial radiative FWHM (eV)	Σ_S/Σ_D
$4s^1$	0	1	4.426	0.291	1.000
	1	1	4.429	0.292	1.001
$3d^9$	1	1	4.527	0.298	1.023
	2	1	3.602	0.237	0.814
	2	2	3.709	0.244	0.838
	3	1	3.754	0.247	0.849
$3p^5$	0	1	3.028	0.199	0.684
	1	1	3.978	0.262	0.899
	1	2	5.156	0.339	1.165
	2	1	3.059	0.201	0.691
$3s^1$	0	1	4.546	0.299	1.027
	1	1	4.559	0.300	1.030
$3d^8$	1/2	1	4.636	0.305	1.048
	1/2	2	4.671	0.307	1.056
	1/2	3	3.094	0.204	0.699
	3/2	1	4.662	0.307	1.054
	3/2	2	4.652	0.306	1.051
	3/2	3	4.670	0.307	1.056
	3/2	4	3.425	0.225	0.774
	5/2	1	4.666	0.307	1.055
	5/2	2	4.651	0.306	1.051
	5/2	3	4.667	0.307	1.055
	5/2	4	2.269	0.149	0.513
	7/2	1	4.670	0.307	1.056
	7/2	2	2.193	0.144	0.496
	7/2	3	2.830	0.186	0.640
	9/2	1	3.602	0.237	0.814
	9/2	2	1.065	0.070	0.241

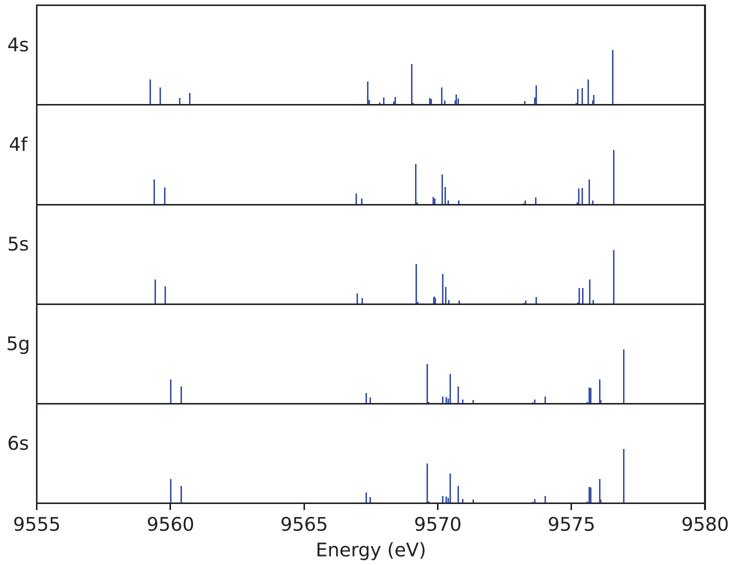

Figure 4. Zinc Kβ $3d^9$ satellite spectrum expanded with the active space 1 $\{3d4s\}$. Several eigenenergies vanish upon the expansion, which may result from abrupt changes in the expansion coefficients of the contributing CSFs. Note the effect on metrics (table 8).

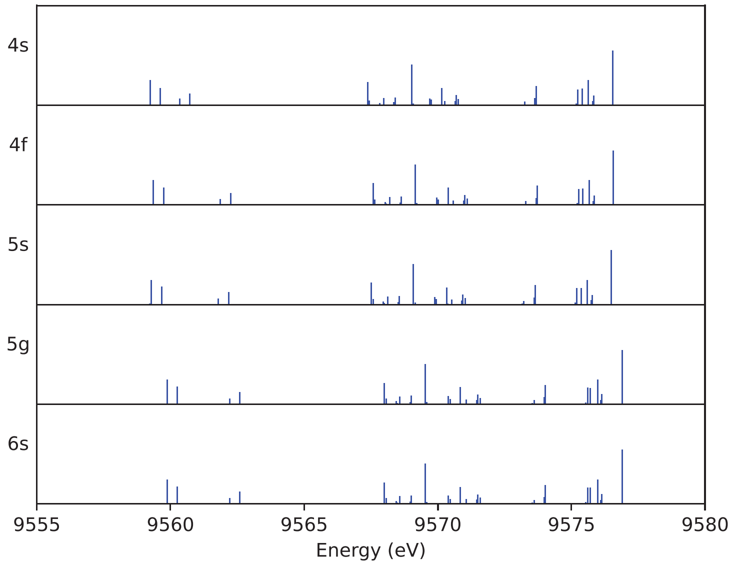

Figure 5. Zinc Kβ $3d^9$ satellite spectrum calculated with active space 2 $\{3s3d\}$. A few eigenenergies near 9561 eV exhibit shifts of order 1 eV when performing single to multiconfiguration expansion. The overall spectral structure is preserved without collapse of eigenenergies. At the 6*s* expansion, the residual energy shifts are well-converged. In contrast to the $\{3d4s\}$ active space, eigenenergies are stable.

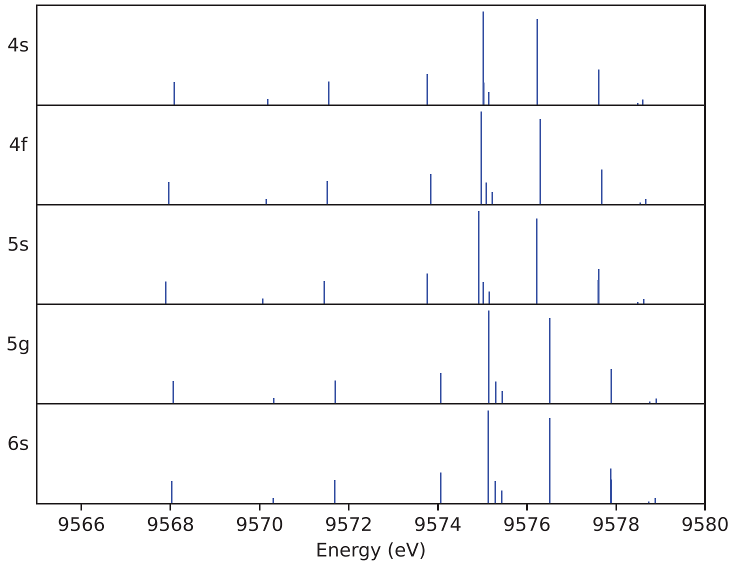

Figure 6. Zinc Kβ $3p^5$ satellite lines calculated using active space 2 $\{3s3d\}$ with virtual orbital expansions up to 6*s*. By the 6*s* expansion, energy shifts are less than 0.1 eV.

in deviations exceeding 30 eV and *A*-coefficient differences of up to 250% between the two expansion methods (see tables 18 and 19 in appendix).

6.3. Summary of each transition using two expansion methods

To ensure proper convergence of our calculations, each transition component (diagram, $4s^1$, $3d^9$, $3p^5$, $3s^1$, and $3d^8$) was evaluated against multiple diagnostic criteria: (i) peak and centre-of-mass energy shifts; (ii) agreement between length and velocity gauge transition rates; (iii) peak and centre-of-mass *A*-coefficient shifts; and (iv) consistency of total dipole rates for any upper state relative to the diagram transition.

Table 12 provides a summary of these diagnostics for the two active-space expansions with: the centre-of-mass energy shift ΔE_{CoM} at the highest orbital expansion; the average gauge ratio of transition rates $A^L_{\mathrm{ave}}/A^V_{\mathrm{ave}}$ at the highest expansion; the percentage variation of the transition rate $\delta A^L_{\mathrm{CoM}}/A^L_{\mathrm{CoM}}$ at the highest orbital expansion; and the largest relative deviation of the dipole transition rate for any upper state from the diagram value, $\mathrm{Max}(\Sigma_S/\Sigma_D)$, within each transition.

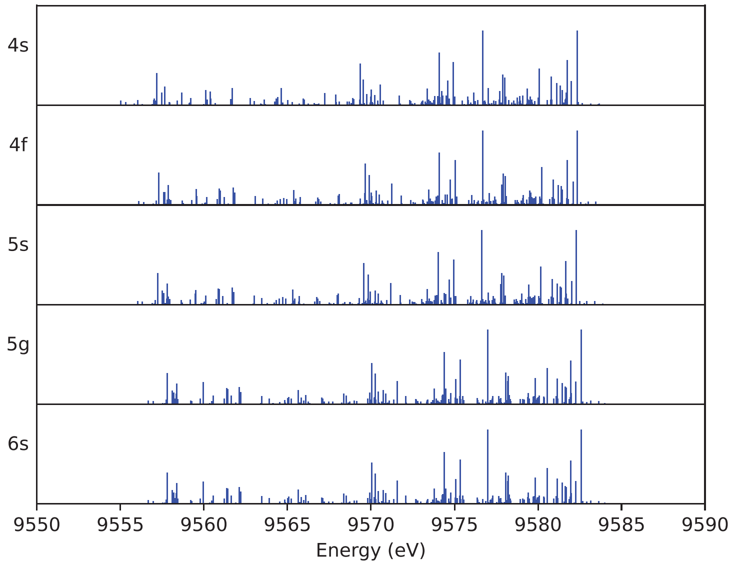

Figure 7. Zinc Kβ $3d^8$ satellite spectrum calculated with active space 2 $\{3s3d\}$. The eigenenergies remain stable across successive orbital expansions, without any collapse of eigenenergy. The resulting spectrum differs markedly from that obtained with the $\{3d4s\}$ active space.

Table 10. Calculated results for zinc Kβ satellite transitions using active space 2 $\{3s3d\}$. Results include single configuration and double excitation. At the highest virtual orbital expansion, eigenenergy shifts remain below 0.05 eV, and $A^L_{\text{ave}}/A^V_{\text{ave}}$ gauge ratios are close to unity. The $3s^1$ satellite exhibits an anomalously large energy shift (35 eV) in the expansion.

Convergence criteria for zinc Kβ satellite transitions calculated with active space 2 $\{3s3d\}$

Expansion		Satellite				
		$4s^1$	$3d^9$	$3p^5$	$3s^1$	$3d^8$
$4s$	Energy (eV)	9568.62	9570.28	9574.92	9575.72	9572.95
	$A^L_{\text{ave}}/A^V_{\text{ave}}$	1.0060	1.0060	1.0049	1.0071	1.0060
$4f$	Energy (eV)	9568.76 (±0.14)	9570.48 (±0.20)	9574.94 (±0.02)	9540.70 (±35.02)	9573.23 (±0.28)
	$A^L_{\text{ave}}/A^V_{\text{ave}}$	1.0060	1.0060	1.0049	0.9995	1.0061
$5s$	Energy (eV)	9568.68 (±0.08)	9570.41 (±0.07)	9574.88 (±0.06)	9541.01 (±0.31)	9573.16 (±0.07)
	$A^L_{\text{ave}}/A^V_{\text{ave}}$	1.0060	1.0060	1.0049	0.9996	1.0060
$5g$	Energy (eV)	9569.19 (±0.51)	9570.87 (±0.46)	9575.14 (±0.26)	9541.62 (±0.61)	9573.56 (±0.40)
	$A^L_{\text{ave}}/A^V_{\text{ave}}$	1.0061	1.0061	1.0049	0.9997	1.0061
$6s$	Energy (eV)	9569.18 (±0.01)	9570.86 (±0.01)	9575.13 (±0.01)	9541.50 (±0.12)	9573.55 (±0.01)
	$A^L_{\text{ave}}/A^V_{\text{ave}}$	1.0061	1.0061	1.0049	0.9997	1.0061
$6g$	Energy (eV)	9569.22 (±0.04)	— —	— —	9541.08 (±0.42)	— —
	$A^L_{\text{ave}}/A^V_{\text{ave}}$	1.0061	—	—	0.9996	—

The diagram and $4s^1$ satellites satisfy all convergence criteria in both AS expansions. The $3s^1$ satellite converges reliably with the $\{3d4s\}$ expansion. The $3d^9$ and $3d^8$ satellites show convergence using the $\{3s3d\}$ expansion. The $3p^5$ satellite exhibits convergence in energy and gauge ratio for both methods; however, its dipole transition rate deviates from the diagram in both expansions. We remind the reader that we have just defined and introduced new metrics as sensitive tests of approach towards convergence and approach towards the relativistic wavefunctions.

Table 11. Active space $\{3d4s\}$ Σ metric: $E1$ decay rates Σ_S for $4s^1$ and $3d^9$ are within 3%, while those for the $3d^8$ are within 7% compared with the diagram transition. $3p^5, 3s^1$ satellites show incomplete convergence.

Summing of A coefficient of Kβ satellite transitions Σ_S with active space 2 $\{3s3d\}$					
Configuration	Initial J	Initial level	$\Sigma_S(10^{14}s^{-1})$	Partial radiative FWHM (eV)	Σ_S/Σ_D
$4s^1$	0	1	4.430	0.292	1.001
	1	1	4.431	0.292	1.001
$3d^9$	1	1	4.554	0.300	1.029
	2	1	4.539	0.299	1.026
	2	2	4.542	0.299	1.027
	3	1	4.553	0.300	1.029
$3p^5$	0	1	3.030	0.199	0.685
	1	1	3.979	0.262	0.899
	1	2	5.161	0.340	1.166
	2	1	3.060	0.201	0.692
$3s^1$	0	1	0.000	0.000	0.000
	1	1	2.842	0.187	0.642
$3d^8$	1/2	1	4.687	0.309	1.059
	1/2	2	4.666	0.307	1.055
	1/2	3	4.683	0.308	1.058
	3/2	1	4.695	0.309	1.061
	3/2	2	4.680	0.308	1.058
	3/2	3	4.689	0.309	1.060
	3/2	4	4.667	0.307	1.055
	5/2	1	4.684	0.308	1.059
	5/2	2	4.672	0.308	1.056
	5/2	3	4.685	0.308	1.059
	5/2	4	4.691	0.309	1.060
	7/2	1	4.672	0.307	1.056
	7/2	2	4.684	0.308	1.059
	7/2	3	4.684	0.308	1.059
	9/2	1	4.694	0.309	1.061
	9/2	2	4.683	0.308	1.058

Table 12. Convergence metrics for zinc Kβ component spectrum, with active spaces 1 $\{3d4s\}$ and 2 $\{3s3d\}$. Components not satisfying convergence criteria are highlighted in bold.

Metric summary of theoretical components calculated using both active spaces						
active space $\{3d4s\}$	Diagram	$4s^1$	$3d^9$	$3p^5$	$3s^1$	$3d^8$
ΔE_{CoM} (eV)	0.01	0.02	0.00	0.00	0.02	**0.19**
$\delta A^L_{\mathrm{CoM}}/A^L_{\mathrm{CoM}}$	0.028%	0.073%	0.010%	0.052%	0.072%	**5.13%**
$A^L_{\mathrm{ave}}/A^V_{\mathrm{ave}}$	1.006	1.006	1.006	1.005	1.007	1.006
Max Σ_S/Σ_D	—	1.001	**0.814**	**0.684**	1.030	**0.241**
active space $\{3s3d\}$	Diagram	$4s^1$	$3d^9$	$3p^5$	$3s^1$	$3d^8$
ΔE_{CoM} (eV)	0.03	0.04	0.01	0.01	**0.42**	0.1
$\delta A^L_{\mathrm{CoM}}/A^L_{\mathrm{CoM}}$	0.11%	0.036%	0.22%	0.23%	0.14%	0.94%
$A^L_{\mathrm{ave}}/A^V_{\mathrm{ave}}$	1.006	1.006	1.006	1.005	1.000	1.006
Max Σ_S/Σ_D	—	1.001	1.026	**0.685**	**0.000**	1.061

7. Comparison with experimental data

7.1. Fitting function

The measured spectra are compared with theoretical predictions that have been convolved with Lorentzian profiles to account for intrinsic lifetime broadening. We define a full theoretical spectrum composed of a superposition of transitions from the set $\mathcal{T} = \{\text{Diagram}, 4s^1, 3d^9, 3p^5, 3s^1, 3d^8\}$, including the primary diagram line and the associated *nl* shake-off satellite transitions:

$$I(E) = S \sum_{t \in \mathcal{T}} P_t I_t(E) \tag{14}$$

where S is a global scaling factor incorporating the total experimental counts, P_t is the relative transition probability, and $I_t(E)$ is the spectral contribution of the tth transition. Note we do not need to include $n = 2$ satellites or $n = 1$ hypersatellites as their spectra lie far from the K$\beta_{1,3}$ spectrum.

Each $I_t(E)$ is given by a weighted sum over n_t normalised Lorentzian profiles, where n_t is the number of energy eigenvalues for the tth transition (i.e. the number of sticks):

$$I_t(E) = \frac{1}{\mathcal{N}_t} \sum_{i}^{n_t} (gf)_{t,i} L_{t,i}(E), \quad L_{t,i}(E) = \sum_{i}^{n_t} \frac{1}{2\pi} \frac{\Gamma_t}{(E - E_{t,i})^2 + \left(\frac{\Gamma_t}{2}\right)^2} \tag{15}$$

where $E_{t,i}$ and $(gf)_{t,i}$ denote the energy eigenvalue (stick position) and weighted oscillator strength (stick intensity), respectively, obtained from Grasp. The parameter Γ_t is the full width at half maximum, treated as a fitting parameter common to each transition t. $\mathcal{N}_t = \sum_i^{n_t} (gf)_{t,i}$ is the normalisation constant, or the total line strength for that transition manifold.

A possible systematic energy offset either due to theoretical calculations or experimental calibration, is accounted for by introducing a free energy shift parameter, δE_t, applied to each transition. The full fitting model for the spectrum is then expressed as:

$$I(E) = S \sum_{t \in \mathcal{T}} \frac{P_t}{\mathcal{N}_t} \sum_{i}^{n_t} \frac{(gf)_{t,i}}{2\pi} \frac{\Gamma_t}{(E - E_{t,i} + \delta E_t)^2 + \left(\frac{\Gamma_t}{2}\right)^2}. \tag{16}$$

7.2. Goodness-of-fit

The quality of the fitting is quantified by the statistical measure of χ_r^2 defined as:

$$\chi_r^2 = \frac{1}{\nu} \sum_{i}^{N} \left(\frac{T_i - E_i}{\sigma_i} \right)^2 \tag{17}$$

where E_i and T_i are the experimental and theoretical-determined values, $\nu = N - p$ is the degree of freedom with N being the number of data points, p being the number of fitting parameters. χ_r^2 of order unity suggests a good fit.

7.3. Hypothesis testing (*F*-test)

Hypothesis testing provides a framework to evaluate if added model complexity is justified. A classic approach for such testing is the *F*-test, which compares nested models based on their fitting quality [23].

Including more free parameters generally reduces χ^2, but this may result from overfitting rather than the genuine physical effects. To determine whether a more complex model, such as one that includes an additional satellite line, provides a significantly better fit, we employ the *F*-test. This test uses the *F*-distribution to quantify whether the observed improvement in fit exceeds what would be expected by chance, for a normally-distributed variate, thereby allowing statistical grounded inference of the underlying physics. The *F*-distribution is:

$$f(F; df_1, df_2) = \frac{\left(\frac{df_1}{df_2}\right)^{\frac{df_1}{2}} F^{\frac{df_1}{2} - 1}}{B\left(\frac{df_1}{2}, \frac{df_2}{2}\right) \left(1 + \frac{df_1}{df_2} F\right)^{\frac{df_1 + df_2}{2}}} \tag{18}$$

where df_j is the degree of freedom for each of the model j, $B(x, y)$ is the beta function, F is the *F*-statistic. The *F*-statistic is computed as:

$$F = \frac{(\chi_1^2 - \chi_2^2) / (p_2 - p_1)}{\chi_2^2 / (N - p_2)} \tag{19}$$

here, N and p denotes the number of data points and fitted parameters respectively, the subscript 1 is the restricted (or reduced) model and 2 is the unrestricted (or extended) model.

The significance level α represents the probability of incorrectly rejecting the null hypothesis (i.e. a false positive). A commonly used threshold is $\alpha = 0.05$, based on which one can determine the critical *F*-value such that the area under the *F*-distribution to its right equals to α. If the computed *F*-statistics exceeds the critical *F*-value, the null hypothesis is rejected in favour of the more complex model.

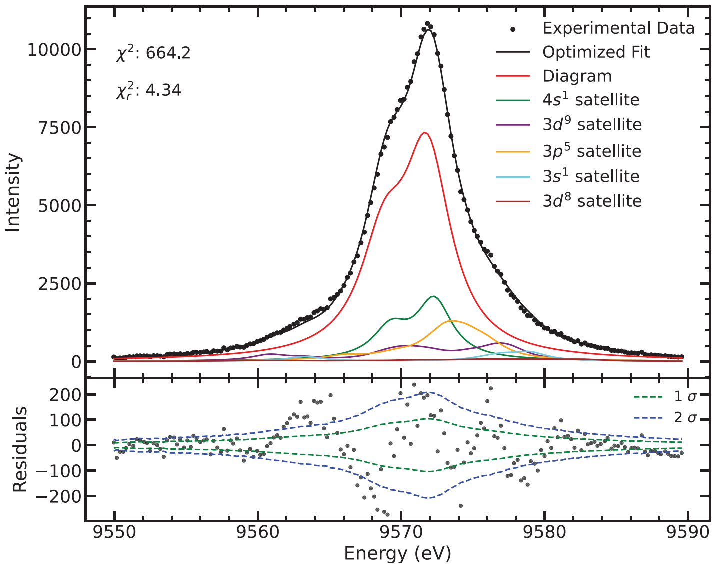

Figure 8. Excellent fit of the Kβ spectrum, including theoretical contributions from the diagram line and $4s^1$, $3d^9$, $3p^5$, $3s^1$, and $3d^8$ satellites. Table 13 lists the fitted values for the FWHM, Γ_t, probabilities P_t, and energy shifts δE_t. $\chi_r^2 = 4.34$.

7.4. Comparison of theory with experiment with free relative amplitudes for each satellite spectrum

Our accurate and converged wavefunctions can be compared with experiment, to investigate the evidence for or against satellite contributions. High-resolution measurements of zinc Kβ emission remain limited in the literature; here, we use the experimental spectrum of Ito *et al* [1] obtained using an antiparallel double-crystal x-ray spectrometer. Instrumental broadening is claimed to be partially removed. The published spectrum was digitised for analysis, yielding 171 data points. Data points are assumed to follow Poisson counting, so that the datum uncertainty for a count N is $\sqrt{N}$. However, this assumes that the original data represented x-ray photons in the count, whereas it is common that they are simply scaled electronic readings. Note from figure 8 that uncertainty at peak is 105 (counts) given by the residual spectrum, and that uncertainty when $N = 1000$ is circa 33, as defined. This can be independently estimated by looking at the local point-to-point variation in regions of no structure, and this is confirmed in the spectrum albeit within a significant uncertainty.

An unconstrained fit of the theoretical spectrum to the digitised experimental data was performed, treating the transition energies (δE_t), relative amplitudes (P_t), Lorentzian full-width-at-half-maximum (Γ_t) as free parameters. Each parameter was loosely restricted to physically meaningful ranges, guided by theoretical shake-off probabilities (table 3). The transition spectra incorporated in the fitting procedure correspond to the most converged results from the two active-space expansions (figure 12): the diagram (D), $4s^1$, and $3s^1$ transitions from the $\{3d4s\}$ expansion, and the $3d^9$, $3p^5$, and $3d^8$ transitions from the $\{3s3d\}$ expansion.

The Kβ spectrum was first fitted using only the diagram (D) transition, followed by the sequential inclusion of satellite lines predicted to be most significant. In order of theoretical importance (table 3), satellites from $4s^1$ and $3d^9$ were included first, followed by $3p^5$, $3s^1$, and $3d^8$. This hierarchical approach enables a stepwise assessment of how each additional satellite affects both the quality of fit and the physical interpretation of the experimental spectrum.

The fit quality improves progressively with the inclusion of additional satellite configurations, with the reduced χ_r^2 decreasing from 49.5 for the diagram-only model to 4.34 for the full model presented (figure 8). The diagram-only fit poorly reproduces the experimental spectrum, whereas the full model successfully captures the major structural features. In the full model, the shoulders of the spectrum are reproduced remarkably well, while the flank region is slightly underfitted, at the high energy tail where the residuals systematically deviates by 2σ, possibly due to an unaccounted background. The fitted spectral intensities of the diagram and $4s^1$ satellite components are highly correlated, suggesting that their true contributions may be obscured by the free-intensity fitting procedure. The fitted intensities of the $3d^9$ and $3s^1$ satellites agree well with theoretical predictions, whereas those of the $3p^5$ and $3d^8$ configurations are approximately twice as large as predicted. The energy shifts are on the order of 1–2 eV.

To assess the statistical significance of each additional satellite component, a series of nested models was constructed, and F-tests were performed to compare each extended model against its corresponding

Table 13. Fitting parameters and goodness-of-fits with free amplitude and independent width parameters, with parameters Γ_t Lorentzian full-width-half-maximum, A_t, fractional intensity, and δE_t, energy shift from fitting various combinations of calculated Zn Kβ diagram and satellite transitions. Values given are for the goodness-of-fit, χ^2 and χ_r^2, widths (FWHM), Γ_t, probability, P_t, and energy shift, δE_t. A positive energy shift defines a shift of energy eigenvalues towards higher energy. † D denotes diagram transition of $1s^{-1} \to 3p^{-1}$ or $[1s] \to [3p]$. ‡ $4s^1$ denotes $4s^1$ satellite lines, that is $1s^{-1}4s^{-1} \to 3p^{-1}4s^{-1}$. * The fitted parameter has hit the bound, the uncertainty is not meaningful, and similarly elsewhere. § The fitted probability of diagram and $4s^1$ satellite components are highly correlated due to their strong spectral overlap, yielding large uncertainty.

Kβ				Transition					
Model	χ^2	χ_r^2	Parameter	diagram	$4s^1$	$3d^9$	$3p^5$	$3s^1$	$3d^8$
Diagram ($D^\dagger$)	8314.1	49.49	Γ_t (eV)	4.00(0.01)*	—	—	—	—	—
			δE_t (eV)	2.00(0.01)	—	—	—	—	—
			P_t (%)	100.0(0.2)	—	—	—	—	—
$D, 4s^{1\ddagger}$	8239.4	49.94	Γ_t (eV)	4.00(0.42)	4.00(1.19)	—	—	—	—
			δE_t (eV)	2.00(0.21)	2.00(1.55)	—	—	—	—
			P_t (%)	74.2(376.3)§	25.8(376.3)§	—	—	—	—
$D, 3d^9$	1260.6	7.64	Γ_t (eV)	4.00(0.03)	—	3.64(0.10)	—	—	—
			δE_t (eV)	1.94(0.01)	—	1.20(0.03)	—	—	—
			P_t (%)	83.4(0.5)	—	16.6(0.5)	—	—	—
$D, 3d^9, 4s^1$	1255.0	7.75	Γ_t (eV)	4.00(0.23)	4.00(1.04)	3.63(0.13)	—	—	—
			δE_t (eV)	1.91(0.37)	2.00(2.75)	1.20(0.03)	—	—	—
			P_t (%)	67.7(375.0)§	15.8(374.9)§	16.5(0.7)	—	—	—
$D, 3d^9, 4s^1$, $3p^5$	765.1	4.81	Γ_t (eV)	3.92(0.50)	3.00(3.22)	3.97(0.19)	3.00(0.65)	—	—
			δE_t (eV)	1.59(0.47)	1.99(1.09)	1.41(0.07)	−2.00(0.16)	—	—
			P_t (%)	62.6(82.4)§	11.1(80.9)§	15.2(0.9)	11.2(2.4)	—	—
$D, 3d^9, 4s^1$, $3p^5, 3s^1$	691.6	4.43	Γ_t (eV)	4.00(0.61)	3.00(2.72)	3.00(0.36)	3.00(0.91)	4.00(0.37)	—
			δE_t (eV)	1.61(0.52)	2.00(0.81)	0.65(0.16)	−2.00(0.18)	−2.00(0.23)	—
			P_t (%)	62.6(89.0)§	14.6(87.2)§	7.7(1.5)	10.2(2.8)	4.8(1.0)	—
$D, 3d^9, 4s^1$, $3p^5, 3s^1, 3d^8$ figure 8	664.2	4.34	Γ_t (eV)	4.00(0.57)	3.00(2.72)	3.00(0.43)	3.00(0.87)	3.00(0.62)	3.00(1.49)
			δE_t (eV)	1.60(0.51)	2.00(0.82)	0.78(0.17)	−2.00(0.19)	−2.00(0.20)	0.73(0.50)
			P_t (%)	62.7(85.6)§	14.1(83.6)§	8.0(1.6)	10.7(2.8)	2.9(1.0)	1.6(0.8)

reduced form. The F-statistic quantifies whether adding new transitions leads to a statistically significant improvement in fitting the experimental data. A statistically significant improvement implies that as the F-statistic exceeds the critical value, the inclusion of the additional satellite component (or any given parameter) results in a *significant improvement* in the fit, (i.e. equivalent to 2 standard error improvement across the spectrum given our choice for the critical value corresponding to a 5% probability for a normally distributed variate). It is therefore highly likely, then, that the additional model component captures genuine spectral structure rather than overfitting.

The F-text results strongly support the inclusion of the $3d^9$ satellite transition, with $F = 307$, confirming its major role in shaping the experimental spectrum. Although the $4s^1$ transition is predicted to contribute notably by shake-off theory, its addition alone is not statistically justified ($F = 0.50$ or $F = 0.24$) due to substantial spectral overlap with the diagram line. Adding $3p^5$ to the $D, 3d^9, 4s^1$ model is also highly significant ($F = 33.9$). The inclusion of $3s^1$ satellite transitions yields modest but statistically meaningful improvement ($F = 5.53$). The inclusion of $3d^8$ transitions yields modest improvement but not significant with $F = 2.10$ (table 14).

Whilst all fitted parameters in table 13 are physically plausible, their uncertainties must be interpreted with caution due to strong parameter correlations, especially between overlapping components (notably D and $4s^1$). More hypothesis testing is called for, as discussed below. The primary objective of this analysis is therefore not to determine precise amplitudes, but to establish, based on both statistical and physical grounds, the existence and necessity of the satellite transitions contributing to the measured spectrum.

7.5. Comparison of theory with experiment using *ab initio* isolated shake probability and pinning

To assess the physical validity of the fitted spectral components, we perform a constrained fit in which the relative intensities of the diagram and satellite transitions are fixed according to *ab initio* shake probability calculations. This approach allows a direct comparison between theory and experiment, avoiding the degeneracies that arise in fully free-intensity models. In particular, the $4s^1$ satellite lies in close

Table 14. F-statistic tests between reduced and extended models for the Kβ spectrum. F-test proves the need for adding $3d^9$ satellites with the diagram spectrum. The $4s^1$ satellite should contribute notably to the spectrum. However, adding $4s^1$ to the nested model $D, 3d^9$ does not yield a statistically significant improvement even though the contribution should be large, because of the strong spectral overlap between the $4s^1$ transitions and the diagram spectrum (figures 1 and 2). Adding $3p^5$ to the extended model ($D, 3d^9, 4s^1$) is important to represent the spectrum. Inclusion of $3s^1$ passes the F-test, implying that all these satellites lie in the experimental spectrum. Inclusion of $3d^8$ makes a modest improvement but may not be significant.

Reduced model	Extended model	Critical F value	F-statistics
D	$D, 4s^1$	2.66	0.50
D	$D, 3d^9$	2.66	307.74
$D, 3d^9$	$D, 4s^1, 3d^9$	2.66	0.24
$D, 4s^1, 3d^9$	$D, 4s^1, 3d^9, 3p^5$	2.66	33.94
$D, 4s^1, 3d^9, 3p^5$	$D, 4s^1, 3d^9, 3p^5, 3s^1$	2.66	5.53
$D, 4s^1, 3d^9, 3p^5, 3s^1$	$D, 4s^1, 3d^9, 3p^5, 3s^1, 3d^8$	2.66	2.10

Table 15. F-statistic tests between reduced and extended models for the Kβ spectrum. F-test proves the need for adding $3d^9$ satellites with the diagram spectrum. The $4s^1$ satellite should contribute notably to the spectrum. However, adding $4s^1$ to the nested model $D, 3d^9$ does not yield a statistically significant improvement even though the contribution should be large, because of the strong spectral overlap between the $4s^1$ transitions and the diagram spectrum (figures 1, 2). Adding $3p^5$ to the extended model ($D, 3d^9, 4s^1$) is important to represent the spectrum. Inclusion of $3s^1$ passes the F-test, implying that all these satellites lie in the experimental spectrum. Inclusion of $3d^8$ makes a modest improvement but may not be significant.

Kβ Model	χ^2	χ_r^2	Parameter	Transition					
				diagram	$3d^9$	$4s^1$	$3p^5$	$3s^1$	$3d^8$
D	36 799.3	217.75	Γ_t (eV)	4.41(0.02)	—	—	—	—	—
			δE_t (eV)	2.00(0.01)	—	—	—	—	—
			P_t(%)	100.0	—	—	—	—	—
$D, 4s^1$	17 250.2	103.29	Γ_t (eV)	4.50(0.51)	4.50(3.33)	—	—	—	—
			δE_t (eV)	2.00(0.27)	2.00(1.76)	—	—	—	—
			P_t(%)	86.8	13.2	—	—	—	—
$D, 4s^1, 3d^9$	3728.1	22.59	Γ_t (eV)	4.22(0.22)	4.45(1.53)	3.00(0.08)	—	—	—
			δE_t (eV)	1.96(0.11)	2.00(0.76)	1.35(0.04)	—	—	—
			P_t(%)	76.9	11.7	11.4	—	—	—
$D, 4s^1, 3d^9, 3p^5$	1263.5	7.75	Γ_t (eV)	4.33(0.07)	3.00(0.27)	3.06(0.11)	3.00(0.30)	—	—
			δE_t (eV)	1.84(0.03)	1.75(0.14)	1.44(0.05)	−1.15(0.16)	—	—
			P_t(%)	73.0	11.1	10.8	5.1	—	—
$D, 4s^1, 3d^9,$ $3p^5, 3s^1$	831.7	5.17	Γ_t (eV)	3.98(0.13)	4.50(1.07)	3.00(0.13)	3.00(0.44)	3.00(0.30)	—
			δE_t (eV)	1.82(0.06)	2.00(0.53)	0.89(0.06)	−1.90(0.23)	−1.35(0.15)	—
			P_t(%)	71.5	10.9	10.6	5.0	2.0	—
$D, 4s^1, 3d^9,$ $3p^5, 3s^1, 3d^8$ figure 9	796.9	5.01	Γ_t (eV)	3.98(0.14)	4.26(1.11)	3.00(0.13)	3.00(0.44)	3.00(0.33)	3.00(1.38)
			δE_t (eV)	1.81(0.07)	2.00(0.55)	0.88(0.06)	−2.00(0.22)	−1.73(0.17)	0.94(0.67)
			P_t(%)	71.0	10.8	10.5	5.0	2.0	0.7

energetic proximity to the main diagram transition and exhibits a highly similar spectral profile, making it difficult for a free intensity fit to distinguish its contribution. The use of theoretical pinning thus provides a more physically grounded model for testing the presence and strength of the $4s^1$ satellites within the experimental spectrum.

The relative spectral weights of the transitions were normalised to the total ensemble probability predicted by theory table 3. The diagram transition dominates the spectrum, contributing approximately 71% of the total normalised intensity. The single shake-off satellites $4s^1$ and $3d^9$ each contribute around 10%, followed by $3p^5$ at 5%, and smaller contributions from $3s^1$ (2%) and $3d^8$ (0.7%). These values define the theoretical population of the initial states responsible for the observed Kβ emission.

The constrained fits show a clear and systematic improvement in fit quality as additional satellite configurations are included, with the corresponding fitting parameters are listed in table 15; $\chi_r^2 = 5.01$ (figure 9), very promising compared with the previous free intensity fitting model. The associated F-statistics (table 16) confirm that each successive extension of the model provides a statistically significant improvement. Even the inclusion of the $3d^8$ double satellite, although it has a small theoretical intensity (0.7%), yields significant statistical improvement ($F = 3.47$), above the critical threshold (3.05), so is confirmed as a significant contribution.

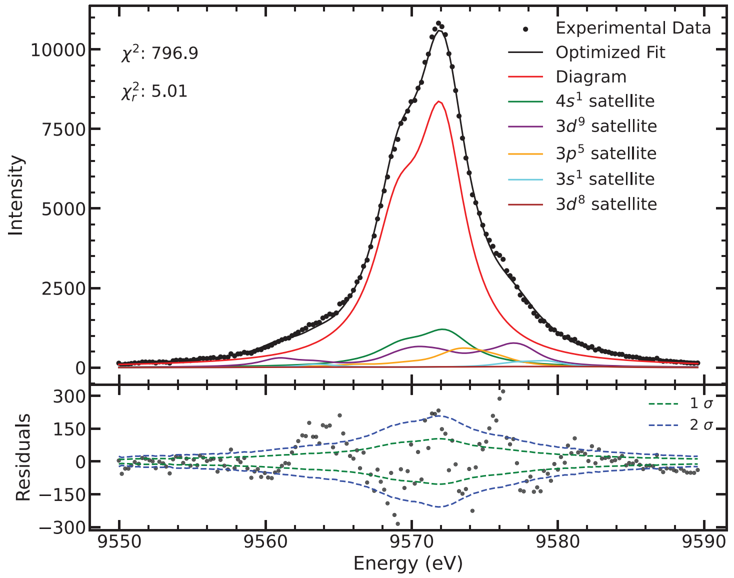

Figure 9. Fit of the Kβ diagram, $4s^1$, $3d^9$, $3p^5$, $3d^8$ and $3s^1$ transitions with intensity pinned by *ab initio* theoretical shake probability (table 15); $\chi_r^2 = 5.01$, promising and consistent with the earlier model fitting with multiple additional free parameters.

Table 16. Results for the F-statistics between the reduced and extended models for Kβ spectrum with intensity pinned by *ab initio* theoretical shake probabilities. All satellites are seen as significant.

Reduced model	Extended model	Critical F value	F-statistics
D	$D, 4s^1$	3.05	94.63
$D, 4s^1$	$D, 4s^1, 3d^9$	3.05	299.23
$D, 4s^1, 3d^9$	$D, 4s^1, 3d^9, 3p^5$	3.05	158.97
$D, 4s^1, 3d^9, 3p^5$	$D, 4s^1, 3d^9, 3p^5, 3s^1$	3.05	41.79
$D, 4s^1, 3d^9, 3p^5, 3s^1$	$D, 4s^1, 3d^9, 3p^5, 3s^1, 3d^8$	3.05	3.47

Note the final χ_r^2 of the theoretical, pinned model is significantly higher than that of the free parameter model. This is expected as the constraints limit non-physical variation of parameters; there are fewer parameters in the model; and there are possible limitations of the theoretical ansatz. The most significant differences between the free fit and the theoretically-constrained fit are the amplitudes for the $3p^5$ satellites and the $3d^8$ satellites, which can be real or artificial and can be due to inadequacies of the complete theoretical model either from the shake probability or, for example, from convergence of the A-coefficients.

7.6. Comparing different AS expansion hypotheses for each eigenvalue and satellite spectrum

The experimental spectrum has been fitted using theoretically determined diagram lines together with the $4s^1$, $3d^9$, $3p^5$, $3s^1$, and $3d^8$ satellite lines, using two different AS expansions: $\{3d4s\}$ and $\{3s3d\}$. The components included in each fit were chosen based on the best convergence metrics (table 12). In particular, the $\{3d4s\}$ expansion yielded well-converged spectra for the diagram (D), $4s^1$, and $3s^1$ transitions, while the $\{3s3d\}$ expansion produced more reliable results for the $3d^9$, $3p^5$, and $3d^8$ satellite manifolds. To assess the sensitivity of the spectral fit to these different AS expansions, four model hypotheses are defined:

1. Model A: D, $4s^1$, and $3s^1$ from $\{3d4s\}$, with $3d^9$, $3p^5$, and $3d^8$ from $\{3s3d\}$ (figure 9).
2. Model B: D, $4s^1$, $3p^5$, and $3s^1$ from $\{3d4s\}$, with $3d^9$ and $3d^8$ from $\{3s3d\}$ (figure 10).
3. Model C: all components obtained solely from the $\{3d4s\}$ AS (figure 11).
4. Model D: all components obtained solely from the $\{3s3d\}$ AS (figure 12).

Figures 9–12 present fitted spectra for all four models, with parameters in table 17. Model A achieved the best overall fit with $\chi_r^2 = 5.01$, closely followed by Model B ($\chi_r^2 = 5.05$). Both models exhibit consistent parameters, as the $3p^5$ satellite transitions are similarly calculated in both expansions.

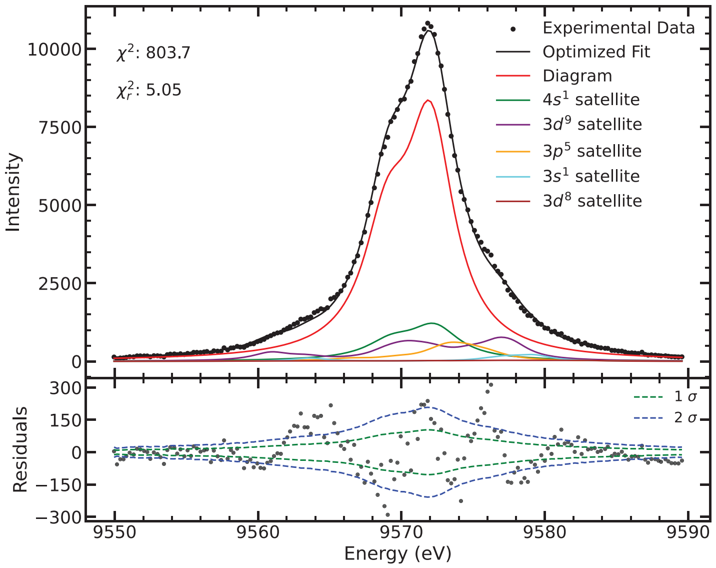

Figure 10. Fit of Model B to the experimental spectrum, combining the D, $4s^1$, $3p^5$, and $3s^1$ transitions from the $\{3d4s\}$ expansion with the $3d^9$ and $3d^8$ transitions from the $\{3s3d\}$ expansion. The fitting parameters are listed in table 17. $\chi_r^2 = 5.05$, comparable to Model A.

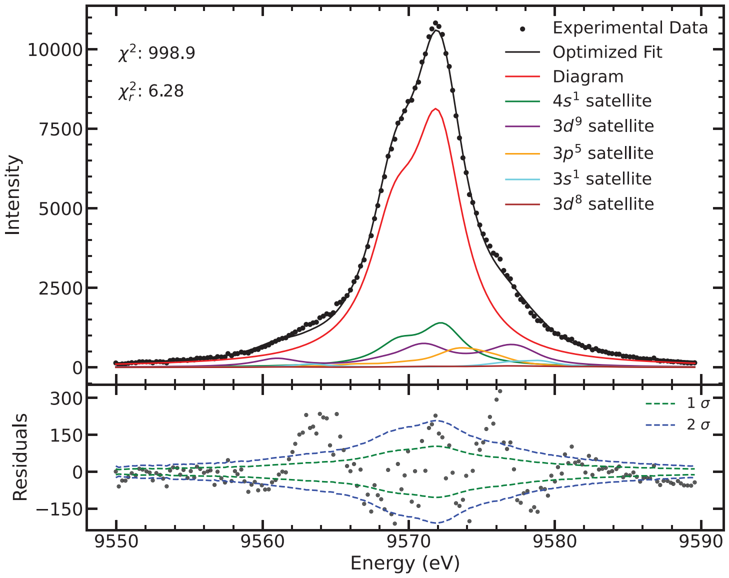

Figure 11. Fit of Model C to the experimental spectrum, combining all transitions (D, $4s^1$, $3d^9$, $3p^5$, $3s^1$, and $3d^8$) from active space 1, $\{3d4s\}$. The fitting parameters are listed in table 17. $\chi_r^2 = 6.28$, not competitive with Models A and B, likely due to the incomplete convergence of the $3d^9$ and $3d^8$ transitions in this method.

Model C, in which all transitions were calculated within the $\{3d4s\}$ expansion, performed less favourably ($\chi_r^2 = 6.28$), consistent with incomplete convergence of the $3d^9$ and $3d^8$ satellite configurations, some eigenenergies were lost during the multiconfiguration expansion. Model D, which relied entirely on the $\{3s3d\}$ expansion, yielded the poorest fit ($\chi_r^2 = 6.96$), likely due to spurious convergence of the $3s^1$ satellite.

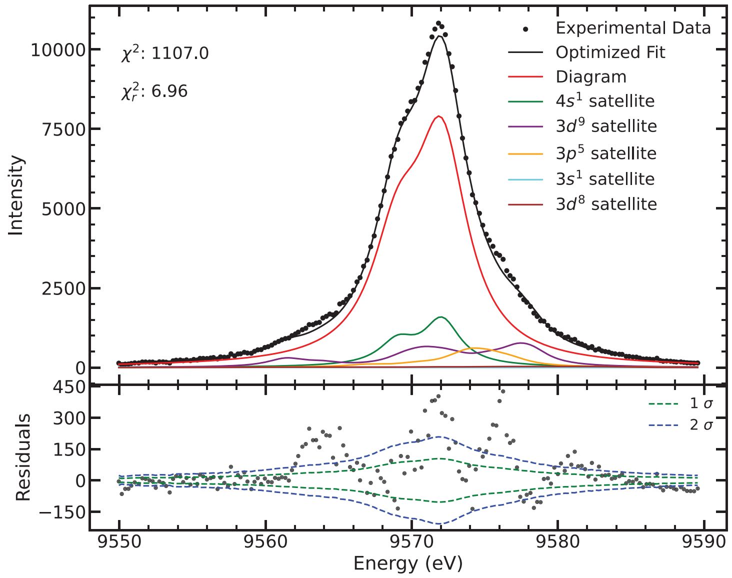

Figure 12. Fit of Model D to the experimental spectrum, combining all transitions (D, $4s^1$, $3d^9$, $3p^5$, $3s^1$, and $3d^8$) from active space 2, $\{3s3d\}$. Table 17 lists fitting parameters. $\chi_r^2 = 6.96$, the highest among the four models. The spectrum is underfitted at the peak and flanks, likely due to spurious convergence of the $3s^1$ transition.

Table 17. Parameters Γ_t Lorentzian full-width-half-maximum, A_t, fractional intensity, and δE_t, energy shift for incorporating satellites from different active space expansions. Included are the goodness-of-fit χ^2, χ_r^2, widths (FWHM), Γ_t, probability, P_t, and energy shift, δE_t.

Kβ				Transition					
Model	χ^2	χ_r^2	Parameter	diagram	$3d^9$	$4s^1$	$3p^5$	$3s^1$	$3d^8$
Model *A*	796.9	5.01	Γ_t (eV)	3.98(0.14)	4.26(1.11)	3.00(0.13)	3.00(0.44)	3.00(0.33)	3.00(1.38)
figure 9			δE_t (eV)	1.81(0.07)	2.00(0.55)	0.88(0.06)	−2.00(0.22)	−1.73(0.17)	0.94(0.67)
			P_t(%)	71.0	10.8	10.5	5.0	2.0	0.7
Model *B*	803.7	5.05	Γ_t (eV)	3.98(0.15)	4.19(1.16)	3.00(0.13)	3.00(0.44)	3.00(0.33)	3.00(1.39)
figure 10			δE_t (eV)	1.81(0.07)	2.00(0.57)	0.88(0.07)	−2.00(0.23)	−1.70(0.17)	0.94(0.67)
			P_t(%)	71.0	10.8	10.5	5.0	2.0	0.7
Model *C*	998.9	6.28	Γ_t (eV)	4.13(0.10)	3.52(0.58)	3.51(0.17)	3.00(0.44)	3.00(0.35)	3.00(1.98)
figure 11			δE_t (eV)	1.80(0.05)	2.00(0.29)	0.78(0.08)	−2.00(0.22)	−2.00(0.18)	0.86(1.00)
			P_t(%)	71.0	10.8	10.5	5.0	2.0	0.7
Model *D*	1107.0	6.96	Γ_t (eV)	4.28(0.07)	3.02(0.29)	3.00(0.11)	3.00(0.34)	3.00(7.50)	3.00(1.41)
figure 12			δE_t (eV)	1.88(0.03)	1.82(0.14)	1.37(0.06)	−1.25(0.16)	−2.00(12.04)	0.88(0.70)
			P_t(%)	71.0	10.8	10.5	5.0	2.0	0.7

8. Conclusion

We have presented the first comprehensive theoretical investigation of the zinc Kβ spectrum. Using the multi-configuration Dirac–Hartree–Fock method, the diagram spectrum, the $[4s], [3d], [3p], [3s]$ single shake transition manifolds, and the $[3d]$ double shake transition spectrum were determined, and these were fitted to the highest accuracy experimental spectra available. We define a series of standard and novel convergence criteria. Each theoretical component was subject to critical convergence metrics. Converged components exhibited energy shifts smaller than 0.03 eV in their expansions, with transition rates in the length and velocity gauges agreeing within 0.6%. Total radiative lifetimes of all components agreed with the diagram transition within 7%, with the exception of the $3p^5$ spectral manifold. Spectral fitting was refined using *ab initio* theoretical shake probabilities. The F-test confirms the significance of all components and the physical reality of all satellite transition spectra.

The inclusion of all spectral contributions discussed yielded χ_r^2 =5.0. The residual plot (figure 9) shows that the majority of data points lie within 1–2 σ of the experimental uncertainties, where the data point uncertainty represented by counting statistics varies from about 30 to 100 across the spectrum as seen on the plot. This excellent agreement lies across the range of the data. A separate series of hypotheses confirmed that the spectrum was best fitted with the well-converged spectra, which is an additional confirmation of the utility and validity of the convergence criteria and the AS expansions.

The present methodology establishes a robust theoretical foundation for interpreting the asymmetry of the K lines in zinc and broadly in $3d$ transition metals, and indeed all complex open-shell atomic systems. The Σ metric offers a sensitive test of the reliability of our calculations. Future work will investigate $[4s3d]$, $[4s3p]$, $[3d3p]$, $[2p]$, $[2s]$ and $[3s^2]$ satellite transition spectra, Auger effects [40, 42, 43], lifetime predictions of widths and profile shapes.

Acknowledgment

This work has been supported by the Australian Research Council Grant No. DP210100795, The University of Melbourne Research Computing Services, and the Petascale Campus Initiative. We acknowledge Jonathan W Dean at the National Institute of Standards and Technology.

Data availability statement

All data that support the findings of this study are included within the article (and any supplementary files).

Author contributions

P H Dong 0009-0004-3327-745X
Data curation (equal), Formal analysis (equal), Investigation (equal), Writing – original draft (equal)

T V B Nguyen
Conceptualization (equal), Investigation (equal), Methodology (equal), Writing – review & editing (equal)

S M Krstevski 0009-0002-2719-4290
Investigation (equal), Methodology (equal), Writing – review & editing (equal)

C T Chantler 0000-0001-6608-0048
Conceptualization (equal), Funding acquisition (equal), Methodology (equal), Project administration (equal), Resources (equal), Software (equal), Supervision (equal), Writing – review & editing (equal)

Appendix. Convergence criteria and *A*-coefficients

Convergence of energy $E_{\text{peak}}, E_{\text{CoM}}$ and transition A coefficient $A_{\text{peak}}, A_{\text{CoM}}$ for each satellite spectrum are tabulated in this appendix. Convergence criteria for each transition obtain in AS 1 $\{3d4s\}$ is given in table 18, where each of the criteria for all transitions appear to stabilise within 0.1% in their highest orbital expansion except for the $3d^8$ double satellite.

In particular the centre-of-mass A coefficient varies by 5%. For the single to multiconfiguration expansion, that is from the $4s$ to the $4f$ level, the centre-of-mass A coefficient changes by 16% for $3d^9$ and 25% for $3d^8$. Convergence criteria for each transition obtained in AS 2 $\{3s3d\}$ is given in table 19. These details are broadly summarised in table 12. The $3d^8$ satellite spectrum has the weakest convergence on the A-coefficient metric and the $\{3s3d\}$ expansion is preferred for this satellite.

Table 18. Convergence criteria for zinc Kβ diagram and satellite transitions calculated with active space 1 $\{3d4s\}$. For each expansion, the peak values correspond to the transition with the largest g_f, while the centre-of-mass (CoM) values are obtained by weighting over all contributing transitions according to their g_f strengths.

	Convergence criteria for zinc Kβ satellite transitions calculated with active space 1 $\{3d4s\}$						
Expansion	Criteria	Diagram	$4s^1$	$3d^9$	$3p^5$	$3s^1$	$3d^8$
$4s$	E_{peak}(eV)	9569.56	9569.76	9576.54	9575.02	9580.32	9576.68
	E_{CoM}(eV)	9568.53	9568.62	9570.28	9574.92	9575.72	9572.95
	$A_{\text{peak}}(10^{11}\text{s}^{-1})$	947.85	790.28	623.83	1247.10	810.86	597.88
	$A_{\text{CoM}}(10^{11}\text{s}^{-1})$	791.01	586.35	332.70	674.26	831.75	229.78
$4f$	E_{peak}(eV)	9569.72(0.16)	9569.87(0.12)	9576.57(0.03)	9575.01(0.01)	9580.43(0.11)	9582.34(5.67)
	E_{CoM}(eV)	9568.69(0.16)	9568.76(0.14)	9570.74(0.46)	9574.97(0.04)	9575.80(0.09)	9573.93(0.98)
	$A_{\text{peak}}(10^{11}\text{s}^{-1})$	937.74(10.11)	782.14(8.14)	619.47(4.36)	1237.31(9.79)	804.13(6.74)	595.57(2.31)
	$A_{\text{CoM}}(10^{11}\text{s}^{-1})$	782.60(8.41)	581.54(4.81)	398.34(65.64)	669.09(5.17)	825.13(6.63)	306.81(77.03)
$5s$	E_{peak}(eV)	9569.74(0.02)	9569.89(0.02)	9576.59(0.02)	9575.02(0.01)	9580.45(0.02)	9582.35(0.01)
	E_{CoM}(eV)	9568.71(0.03)	9568.78(0.02)	9570.76(0.02)	9574.98(0.01)	9575.83(0.02)	9573.96(0.03)
	$A_{\text{peak}}(10^{11}\text{s}^{-1})$	937.35(0.39)	781.93(0.21)	619.19(0.27)	1239.27(1.96)	803.74(0.39)	595.27(0.31)
	$A_{\text{CoM}}(10^{11}\text{s}^{-1})$	782.27(0.32)	581.06(0.48)	396.92(1.42)	669.90(0.81)	824.77(0.36)	304.37(2.44)
$5g$($5d$ for $3d^8$)	E_{peak}(eV)	9570.21(0.47)	9570.34(0.45)	9576.95(0.36)	9575.21(0.19)	9580.93(0.48)	9582.29(0.06)
	E_{CoM}(eV)	9569.19(0.48)	9569.25(0.47)	9571.16(0.40)	9575.22(0.24)	9576.26(0.44)	9573.77(0.19)
	$A_{\text{peak}}(10^{11}\text{s}^{-1})$	932.54(4.82)	778.31(3.62)	618.59(0.61)	1234.30(4.97)	800.98(2.76)	594.78(0.49)
	$A_{\text{CoM}}(10^{11}\text{s}^{-1})$	778.22(4.05)	579.67(1.39)	395.33(1.59)	667.57(2.34)	821.81(2.96)	289.50(14.86)
$6s$	E_{peak}(eV)	9570.22(0.01)	9570.35(0.01)	9576.96(0.00)	9575.21(0.00)	9580.94(0.01)	—
	E_{CoM}(eV)	9569.20(0.01)	9569.26(0.01)	9571.17(0.00)	9575.22(0.00)	9576.27(0.01)	—
	$A_{\text{peak}}(10^{11}\text{s}^{-1})$	932.27(0.26)	778.24(0.07)	618.49(0.10)	1233.93(0.37)	800.82(0.15)	—
	$A_{\text{CoM}}(10^{11}\text{s}^{-1})$	778.00(0.22)	579.52(0.16)	395.36(0.04)	667.38(0.19)	821.63(0.17)	—
$6g$	E_{peak}(eV)	—	9570.38(0.02)	—	9575.22(0.00)	9580.95(0.01)	—
	E_{CoM}(eV)	—	9569.28(0.02)	—	9575.22(0.00)	9576.29(0.02)	—
	$A_{\text{peak}}(10^{11}\text{s}^{-1})$	—	777.73(0.52)	—	1233.25(0.68)	800.59(0.24)	—
	$A_{\text{CoM}}(10^{11}\text{s}^{-1})$	—	579.10(0.42)	—	667.03(0.35)	821.04(0.59)	—

Table 19. Convergence criteria for zinc Kβ diagram and satellite transitions calculated with active space 2 $\{3s3d\}$. For each expansion, the peak values correspond to the transition with the largest g_f, while the centre-of-mass (CoM) values are obtained by weighting over all contributing transitions according to their g_f strengths.

Convergence criteria for zinc Kβ satellite transitions calculated with active space 2 $\{3s3d\}$							
Expansion	Criteria	Diagram	$4s^1$	$3d^9$	$3p^5$	$3s^1$	$3d^8$
$4s$	$E_{\mathrm{peak}}(\mathrm{eV})$	9569.56	9569.76	9576.54	9575.02	9580.32	9576.68
	$E_{\mathrm{CoM}}(\mathrm{eV})$	9568.53	9568.62	9570.28	9574.92	9575.72	9572.95
	$A_{\mathrm{peak}}(10^{11}\mathrm{s}^{-1})$	947.85	790.28	623.83	1247.10	810.86	597.88
	$A_{\mathrm{CoM}}(10^{11}\mathrm{s}^{-1})$	791.01	586.35	332.70	674.26	831.75	229.78
$4f$	$E_{\mathrm{peak}}(\mathrm{eV})$	9569.71(0.15)	9569.87(0.11)	9576.57(0.03)	9574.98(0.04)	9539.89(40.44)	9582.34(5.67)
	$E_{\mathrm{CoM}}(\mathrm{eV})$	9568.68(0.15)	9568.76(0.13)	9570.48(0.20)	9574.94(0.02)	9540.70(35.02)	9573.23(0.28)
	$A_{\mathrm{peak}}(10^{11}\mathrm{s}^{-1})$	937.67(10.18)	782.27(8.01)	619.87(3.96)	1237.66(9.44)	259.07(551.80)	595.83(2.05)
	$A_{\mathrm{CoM}}(10^{11}\mathrm{s}^{-1})$	782.54(8.47)	581.90(4.45)	329.15(3.55)	669.22(5.04)	228.52(603.23)	228.85(0.94)
$5s$	$E_{\mathrm{peak}}(\mathrm{eV})$	9569.63(0.08)	9569.79(0.08)	9576.50(0.08)	9574.92(0.06)	9540.20(0.32)	9582.27(0.07)
	$E_{\mathrm{CoM}}(\mathrm{eV})$	9568.60(0.08)	9568.68(0.08)	9570.41(0.07)	9574.88(0.07)	9541.01(0.31)	9573.16(0.07)
	$A_{\mathrm{peak}}(10^{11}\mathrm{s}^{-1})$	936.70(0.97)	781.50(0.77)	619.28(0.59)	1242.31(4.65)	258.75(0.32)	595.33(0.50)
	$A_{\mathrm{CoM}}(10^{11}\mathrm{s}^{-1})$	781.73(0.81)	581.11(0.79)	327.96(1.19)	671.15(1.93)	228.05(0.48)	229.82(0.98)
$5g$	$E_{\mathrm{peak}}(\mathrm{eV})$	9570.14(0.51)	9570.28(0.49)	9576.89(0.40)	9575.15(0.23)	9545.45(5.25)	9582.57(0.30)
	$E_{\mathrm{CoM}}(\mathrm{eV})$	9569.12(0.52)	9569.19(0.51)	9570.87(0.46)	9575.14(0.26)	9541.62(0.60)	9573.56(0.40)
	$A_{\mathrm{peak}}(10^{11}\mathrm{s}^{-1})$	933.34(3.36)	778.79(2.71)	618.62(0.66)	1238.61(3.70)	271.29(12.54)	595.18(0.15)
	$A_{\mathrm{CoM}}(10^{11}\mathrm{s}^{-1})$	778.91(2.82)	580.69(0.42)	325.70(2.26)	669.32(1.83)	233.29(5.25)	235.34(5.52)
$6s$	$E_{\mathrm{peak}}(\mathrm{eV})$	9570.14(0.00)	9570.27(0.01)	9576.88(0.01)	9575.13(0.02)	9545.33(0.11)	9582.56(0.01)
	$E_{\mathrm{CoM}}(\mathrm{eV})$	9569.12(0.00)	9569.18(0.01)	9570.86(0.01)	9575.13(0.01)	9541.50(0.11)	9573.55(0.01)
	$A_{\mathrm{peak}}(10^{11}\mathrm{s}^{-1})$	933.21(0.13)	778.69(0.10)	618.59(0.03)	1235.20(3.41)	271.16(0.13)	595.17(0.01)
	$A_{\mathrm{CoM}}(10^{11}\mathrm{s}^{-1})$	778.80(0.11)	580.60(0.09)	326.43(0.72)	667.81(1.51)	233.34(0.05)	233.15(2.19)
$6g$	$E_{\mathrm{peak}}(\mathrm{eV})$	9570.17(0.03)	9570.30(0.03)	—	—	9544.91(0.43)	—
	$E_{\mathrm{CoM}}(\mathrm{eV})$	9569.15(0.03)	9569.22(0.03)	—	—	9541.08(0.42)	—
	$A_{\mathrm{peak}}(10^{11}\mathrm{s}^{-1})$	932.22(0.99)	778.04(0.65)	—	—	271.90(0.74)	—
	$A_{\mathrm{CoM}}(10^{11}\mathrm{s}^{-1})$	777.96(0.83)	580.39(0.21)	—	—	233.66(0.32)	—

References

[1] Ito Y *et al* 2018 *Phys. Rev. A* **97** 052505
[2] Gottwald M, Parmar A N, Reynolds A P, White N E, Peacock A and Taylor B G 1995 *Astron. Astrophys. Suppl. Ser.* **109** 9–28
[3] Asai K, Dotani T, Nagase F and Mitsuda K 2000 *Astrophys. J. Suppl. Ser.* **131** 571
[4] Finocchiaro G, Naselli E, Mishra B, Biri S, Mazzaglia M, Pidatella A, Rácz R, Torrisi G and Mascali D 2024 *Phys. Plasmas* **31** 062506
[5] Omar H D 2016 *Int. Lett. Chem. Phys. Astron.* **64** 130
[6] Potts P J, Webb P C and Williams-Thorpe O 1997 *J. Anal. At. Spectrom.* **12** 769
[7] Kubin M *et al* 2017 *Struct. Dyn.* **4** 054307
[8] Barkla C G 1911 *London, Edinburgh Dublin Phil. Mag. J. Sci.* **22** 396
[9] Moseley H G J 1914 *London, Edinburgh Dublin Phil. Mag. J. Sci.* **27** 703
[10] Meldner H W and Perez J D 1971 *Phys. Rev. A* **4** 1388
[11] Carlson T A, Nestor C W, Tucker T C and Malik F B 1968 *Phys. Rev.* **169** 27
[12] Carlson T A and Nestor C W 1973 *Phys. Rev. A* **8** 2887
[13] Coster D and de Laer Kronig R 1935 *Physica* **2** 13
[14] Srivastava K S, Shrivastava R L, Harsh O K and Kumar V 1979 *Phys. Rev. B* **19** 4336
[15] Srivastava K S, Singh S, Srivastava A K, Nayal R S, Chaubey A and Gupta P 1982 *Phys. Rev. A* **25** 2838
[16] Doniach S and Sunjic M 1970 *J. Phys. C* **3** 285
[17] Finster J, Leonhardt G and Meisel A 1971 *J. Phys. Colloq.* **32** C4
[18] Krause M O and Oliver J H 1979 *J. Phys. Chem. Ref. Data* **8** 329
[19] Campbell J L and Papp T 2001 *At. Data Nucl. Data Tables* **77** 1
[20] Deutsch M, Hölzer G, Härtwig J, Wolf J, Fritsch M and Förster E 1995 *Phys. Rev. A* **51** 1
[21] Chantler C T, Lowe J A and Grant I P 2013 *J. Phys. B: At. Mol. Opt. Phys.* **46** 015002
[22] Nguyen T V B, Melia H A, Janssens F I and Chantler C T 2022 *Phys. Lett. A* **426** 127900
[23] Dean J W, Melia H A, Nguyen T V B and Chantler C T 2024 *Phys. Rev. A* **109** 022809
[24] Dyall K, Grant I, Johnson C, Parpia F and Plummer E 1989 *Comput. Phys. Commun.* **55** 425
[25] Parpia F, Fischer C and Grant I 1996 *Comput. Phys. Commun.* **94** 249
[26] Grant I, McKenzie B, Norrington P, Mayers D and Pyper N 1996 *Comput. Phys. Commun.* **96** 323
[27] Jönsson P, He X, Fischer C F and Grant I P 2007 *Comput. Phys. Commun.* **177** 597
[28] Lowe J A, Chantler C T and Grant I P 2013 *Radiat. Phys. Chem.* **85** 118
[29] Jönsson P, Gaigalas G, Bieroń J, Froese-Fischer C and Grant I P 2013 *Comput. Phys. Commun.* **184** 2197

[30] Nguyen T V B, Lowe J A, Pham T L H, Grant I P and Chantler C T 2023 *Radiat. Phys. Chem.* **204** 110644
[31] Lowe J A, Chantler C T and Grant I P 2011 *Phys. Rev. A* **83** 060501
[32] Nguyen T V B, Melia H A, Janssens F I and Chantler C T 2022 *Phys. Rev. A* **105** 022811
[33] Nguyen T V B, Krstevski S and Chantler C T 2025 (in preparation)
[34] Chantler C T, Hayward A C L and Grant I P 2009 *Phys. Rev. Lett.* **103** 123002
[35] Pham T L H, Nguyen T V B, Lowe J A, Grant I P and Chantler C T 2016 *J. Phys. B: At. Mol. Opt. Phys.* **49** 035601
[36] Krstevski S, Nguyen T V B and Chantler C T 2025 *Phys. Rev. A*
[37] Grant I P 1974 *J. Phys. B: At. Mol. Opt. Phys.* **7** 1458
[38] Fischer C F 2009 *Phys. Scr.* **2009** 014019
[39] Chantler C T, Lowe J A and Grant I P 2010 *Phys. Rev. A* **82** 052505
[40] Dean J W, Thompson S N and Chantler C T 2024 *Molecules* **29** 4199
[41] Dean J W, Pushkarna P, Melia H A, Nguyen T V B and Chantler C T 2022 *J. Phys. B: At. Mol. Opt. Phys.* **55** 075002
[42] Melia H A, Chantler C T, Smale L F and Illig A J 2020 *J. Phys. B: At. Mol. Opt. Phys.* **53** 195002
[43] Melia H A, Dean J W, Nguyen T V B and Chantler C T 2023 *Phys. Rev. A* **107** 012809